Check for updates

Accepted Article

Blowing Snow at McMurdo Station, Antarctica during the AWARE Field Campaign: Surface and Ceilometer Observations

Nicole A. Loeb[1] and Aaron Kennedy[2]

[1]Department of Environment and Geography, University of Manitoba

[2]Department of Atmospheric Sciences, University of North Dakota

Corresponding author: Aaron Kennedy (aaron.kennedy@und.edu)

Key Points:

- The frequency of blowing snow at McMurdo Station, Antarctica is analyzed based on human observations and ground-based instrumentation.
- Alterations to the algorithm developed by Gossart et al. (2017) are presented to increase confidence in detection of blowing snow.
- Parsivel[2] laser disdrometer observations have an unrealistic dependence on wind speed during blowing snow events.

This article has been accepted for publication and undergone full peer review but has not been through the copyediting, typesetting, pagination and proofreading process, which may lead to differences between this version and the Version of Record. Please cite this article as doi: 10.1029/2020JD033935.

This article is protected by copyright. All rights reserved.

Accepted Article

Abstract

Blowing snow is an impactful process in cold climates, affecting regional thermodynamics, radiation properties, and the surface mass balance of snow. Though it has significant climatic impacts, the process is still poorly understood and not widely included in weather and climate models. In 2016, the AWARE Field Campaign saw the deployment of a large suite of in situ and remote sensing instruments to McMurdo Station, Antarctica allowing for investigation of blowing snow. A ceilometer-based blowing snow detection algorithm used elsewhere in Antarctica is applied to data from AWARE, yielding a blowing snow frequency of 14.1% compared to 8.2% as detected by human observers. To increase confidence in detections, the algorithm is updated to have shorter temporal averaging and to include a variety of meteorological thresholds to limit false detections due to fog. Efforts to incorporate a laser disdrometer into the algorithm were unsuccessful. An unphysical dependence of particle size distributions on wind speed is found suggesting observations are problematic at wind speeds greater than 10 m s^{-1}. The revised algorithm detected a blowing snow frequency of 7.4%, increasing agreement with human observations and confidence that the process is actively occurring at the observation site. These observations are put into context of a climatology of human observations of blowing snow at McMurdo station from 2002-2018. An annual average of 8.0-14.0% is estimated, with a total annual range of 3.4-21.3%. Regardless of whether blowing snow is observed by humans or instrument, the majority of cases at this location are associated with ongoing precipitation.

1 Introduction

The movement of surface snow by the wind is a common phenomenon in high latitude regions, and is often referred to as snow transport (Li & Pomeroy, 1997). The redistribution of surface snow is typically broken down into two processes: blowing and drifting. The distinction between these two types of snow transport is the height at which the process occurs. Mahesh et al. (2003) defines blowing snow (hereafter BLSN) as “masses of snow particles carried by the wind to fill the near-surface atmospheric layer and to limit horizontal visibility”. The Atmospheric Environment Service (part of Environment and Climate Change Canada) states that blowing snow obscures visibility from the surface up to 9.7 km altitude (Li & Pomeroy, 1997). Drifting snow only includes events where the transportation layer is restricted to the lowest 2 m above the surface (Gossart et al., 2017; Leonard et al., 2012; Li & Pomeroy, 1997). These definitions are consistent with those given by the American Meteorological Society Glossary of Meteorology, although the National Weather Service (NWS) often states "eye-level" vs. providing an exact height as the distinction between the two processes (NOAA, 1998).

The transportation of snow has numerous impacts in cold climate regions. From a radiation budget perspective, BLSN plumes can increase the albedo over the surface and reduce the surface temperature which in turn increases the stability of the surface inversion layer (Bintanja, 2001; Leonard et al., 2012; Yang & Yau, 2011). This effect depends on the surface in which the snow is blowing over. The depth of the BLSN plume affects the behavior of longwave radiation, altering the depth of the surface inversion (Mahesh et al., 2003).

BLSN also has a number of thermodynamic and kinematic impacts in the boundary layer. Particles in the air increase friction and resistance, having a strong impact on vertical wind speed gradients (Bintanja, 2001). Thermodynamically, BLSN is associated with increased sublimation rates. As particles are lifted, a higher proportion of each particle’s surface area is exposed to the air, increasing the rate at which particles may sublimate if the relative humidity is less than 100% (Déry & Yau, 2002; Palm et al., 2017). The extent of sublimation varies depending on the size and quantity of particles suspended in the air, as well as the temperature and humidity of the layer (Palm et al., 2017). Smaller particles, which are more likely aloft, sublimate faster than the larger particles found near the surface due to drier air and their higher surface area to mass ratio (Pomeroy & Male, 1988). Sublimation may be increased by up to 80% due to entrainment or advection of dry air into a BLSN plume (Bintanja, 2001). Estimations of total mass loss due to sublimation of BLSN have been calculated based on satellite retrievals (e.g. Palm et al., 2017).

Finally, BLSN has ramifications for the surface water budget. BLSN modifies the properties of the surface snow pack by transportation and sublimation (Bintanja & Reijmer, 2001; Budd, 1966; Déry & Yau, 2002; Lenaerts et al., 2010). This process can significantly impact the local surface mass balance in regions where BLSN is common, such as Antarctica. For example, BLSN sublimation and transport combined is estimated to remove over 50% of fallen snow in some coastal regions of Antarctica (Scarchilli et al., 2010). Palm et al. (2017) estimated that the Antarctic continent loses an average of 393.4 ± 197 Gt of snow annually due to BLSN sublimation.

This article is protected by copyright. All rights reserved.

Accepted Article

A variety of remote sensing projects have been performed to better observe and understand BLSN. These include ground-based studies with lidar and radar (e.g. Mahesh et al. 2003; Bourdages et al. 2009; Gossart et al. 2017), and satellite-based studies (e.g. Palm et al. 2011, 2017, 2018). Ground-based studies have no obstruction due to cloud cover, whereas satellite-based studies are limited to cloud-free BLSN events, which are less frequent over the coastal regions of Antarctica (Adhikari et al., 2012; Listowski et al., 2019). Gossart et al. (2020) estimated that 90% of BLSN in coastal Antarctica occurs during cloudy conditions, and is likely missed by satellite. Satellite studies allow a broader spatial understanding of the process, as measurements are made over broad geographic areas, while ground-based studies allow for better characterization of the boundary layer based on a single location.

Gossart et al. (2017) developed an algorithm to detect BLSN based on backscatter profiles from a ground-based ceilometer. Ceilometer data was analyzed at Neumayer III and Princess Elisabeth stations in eastern Antarctica from 2010 to 2016. The algorithm agreed with human observations of BLSN 78% of the time. At these locations, availability of fresh snow was as important as wind speed, as 92% of BLSN observed occurred during or shortly after fresh snowfall from synoptic-scale events.

The frequency of BLSN varies across Antarctica due to topography and regional climate dynamics. Human observations indicate that BLSN occurs 33.8% of the time at the South Pole Station, with annual frequencies ranging from 22.1% to 53.3% (Mahesh et al., 2003). Based on satellite retrievals, Palm et al. (2018) calculated megadune regions of the ice sheet can see frequencies up to 75% while coastal locations were lower. Moisture and clouds are more bountiful in coastal regions allowing for increased precipitation compared to the inland portions of the continent. This poses obscuration problems for satellite-based studies. For example, Palm et al. (2018) estimated frequencies could be artificially lower in these areas by 25-30%. Many BLSN events occur within 24-48 hours of a precipitation event, suggesting that the coastal regions may see increased BLSN than otherwise suggested from satellite studies (Gossart et al., 2017).

Although the effects of BLSN are vital to understanding the climate of high latitude regions, this phenomenon is still poorly understood and not widely included in weather and climate models (Gallée et al., 2001; Agosta et al., 2019). While BLSN models exist to simulate plumes and regional surface mass balance, there are large uncertainties. A primary issue limiting the accuracy of these models, and the ability to correctly parameterize the process in weather and climate models, is a lack of observations and understanding of the process itself (Trouvilliez et al., 2014). The varying parameterizations bring difficulty to modeling the surface mass balance of ice sheets in the polar regions (Leonard et al., 2012). Better understanding of the process will allow for the improvements of model parameterizations and estimates of snow transport and sublimation.

The U.S. Department of Energy (DOE) Atmospheric Radiation Measurement (ARM) West Antarctic Radiation Experiment (AWARE) Field Campaign took place in 2016 to investigate cryospheric loss in the West Antarctic Ice Sheet (WAIS). McMurdo Station on Ross Island (77°51'S, 166°40'E) was the central facility for the project, with an additional mobile facility deployed at the WAIS (79°28'S, 112°5'W) during the summer (Lubin et al., 2020). The locations of the sites are shown in Figure 1. The full ARM Mobile Facility (AMF2) was deployed to McMurdo Station for all of 2016 including approximately 50 in situ and remote sensing instruments. To date, this allows for the most comprehensive look at the surface energy budget and thermodynamic structure of the atmosphere in Western Antarctica (Lubin et al., 2020). Priority was placed on studying the importance of mixed-phased clouds and aerosols with respect to the radiation budget and understanding cloud microphysical properties (Lubin et al., 2015). While understanding BLSN in the region was not explicitly a goal of the campaign, AWARE provides a unique opportunity to study the process with a wide variety of instrumentation deployed for a full year, supplying continuous, quality-controlled data.

The work provided herein is the first part of a series of papers to investigate observations and simulations of BLSN at McMurdo Station. In this initial study, surface and ceilometer observations provided by the AMF2 during the 2016 AWARE campaign are used to identify the frequency of BLSN at McMurdo Station. The Gossart et al. (2017) ceilometer based BLSN algorithm is applied to observations and adjusted to ensure confidence in BLSN detection at this location. These observations are contextualized by investigating the climatology of BLSN at McMurdo Station using human observations.

This article is protected by copyright. All rights reserved.

Accepted Article

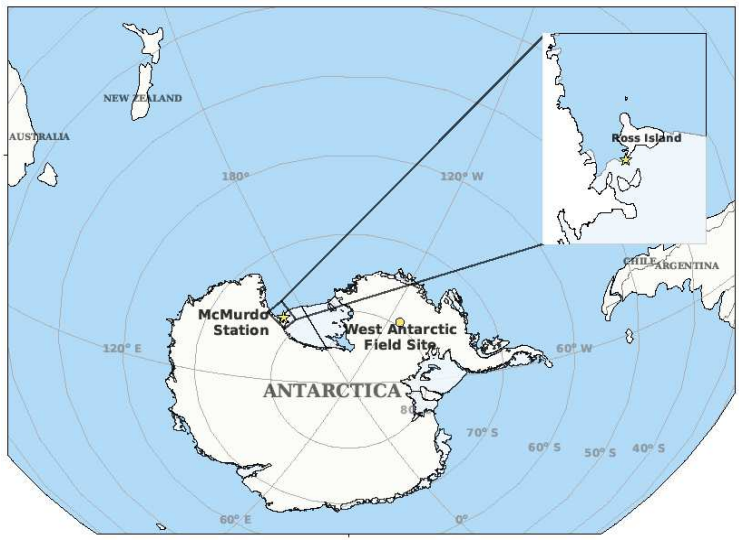

Figure 1. Map showing the location of McMurdo Station and the Western Antarctic Ice Sheet field site.

2 Human Observations of BLSN

Surface weather conditions are recorded by human observers within McMurdo Station for three-hour periods. These observations are available from 1999 to present from the Antarctic Meteorological Research Center (AMRC) at the University of Wisconsin-Madison. For the purposes of this study, only complete years of records from 2002-2018 were analyzed. Freezing precipitation (snow, snow grains, or ice crystals; SN/SG/IC), fog/mist (FG/BR), and BLSN conditions are recorded as the length of time for each three-hour period that said condition occurred.

The 17 years of human observations from McMurdo Station are used as context for observations taken during AWARE. While there are no major issues with understanding the climatology of human observed BLSN using this data, several potential issues need to be considered when comparisons are made to instrumentation at the AMF2. First, human observations are made in town (10 m elevation) while the AMF2 was deployed near the observation hill southeast of McMurdo Station (78 m elevation). The complex terrain of Ross Island suggests that location alone could cause some differences. Human observations also have a degree of subjectivity; observations may be inconsistent between different observers and human error is possible even from the standpoint of simple data entry (Elevant, 2010; Hanesiak & Wang, 2005). Additionally, it is dark in Antarctica for approximately half of the year, making it more difficult to observe surface conditions as noted in other high latitude studies (Hanesiak & Wang, 2005). Collectively, it is probable that the human observed frequency of BLSN at McMurdo Station is biased when compared to observations at the AMF2.

The daily observer spreadsheets from McMurdo Station were accessed from the AMRC repository for 2002-2018. The date, hours, and timing of each weather condition from each daily worksheet were aggregated into comma delimited files to compare with algorithm results. The amount of BLSN was then broken down into times including occurrence with other phenomena.

2.1. Climatology at McMurdo Station

From 2002 to 2018, McMurdo Station had an annual average of 806.9 hours of BLSN, yielding a frequency of 9.2% (Figure 2). The frequency of BLSN has substantial variability at this location with totals ranging from 371.0 to 1214.2 hours (4-14%, Figure 2a). BLSN varies by season with maximum frequencies during the austral winter (April - October, Figure 2b). Overall, June is the climatological maximum for BLSN with an average of 118.6 hours (16.4%). Conversely, very little BLSN occurs during the summer months of December – February. For example, the December average for BLSN is 11.3 hours (1.6%). Between these seasons, transitional periods are observed, however, the greatest variability occurs at the end of the cold season (September and October).

This article is protected by copyright. All rights reserved.

Accepted Article

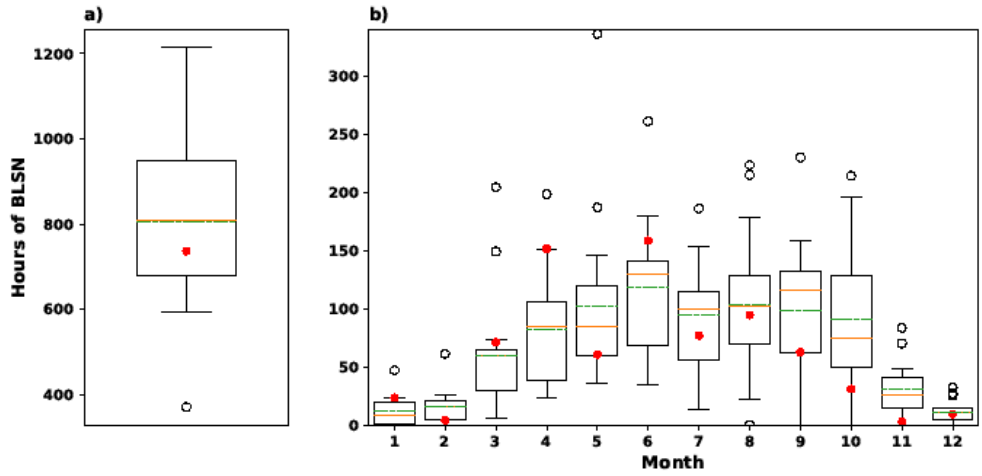

Figure 2. Boxplots showing distribution of a) annual and b) monthly frequencies of BLSN from human observations at McMurdo Station. The orange solid and green dashed lines represent the median and mean of the distribution, respectively. Red dots show the observed frequency in 2016 during the AWARE Campaign.

Observations of BLSN were investigated by its occurrence with other conditions (Figure 3). The majority of all BLSN observations occur concurrently with falling solid precipitation in all seasons. This is particularly the case during summer, accounting for an average of 78% of BLSN observations. This proportion falls to 56-63% during the rest of the year, as more BLSN is observed by itself.

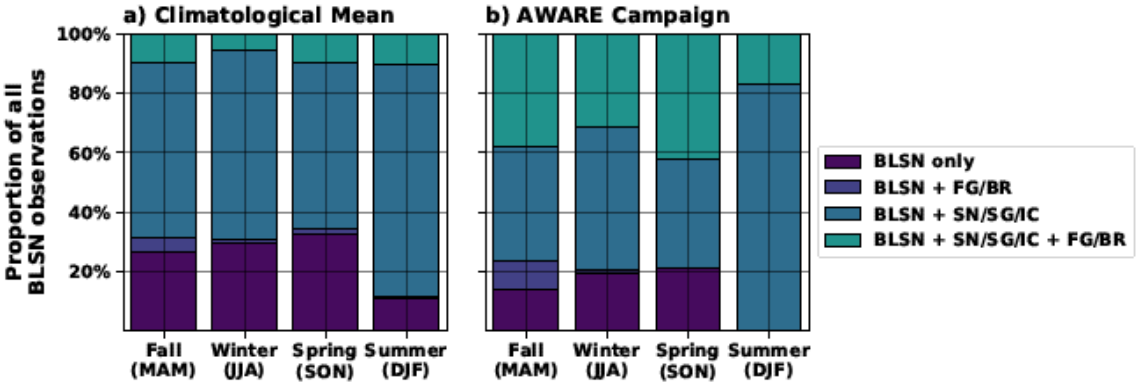

Figure 3. Seasonal proportion of human BLSN observations occurring with other phenomena at McMurdo Station for the a) 2002-2018 climatological average and b) AWARE campaign.

2.2. Human Observations during AWARE

BLSN during the AWARE Campaign was slightly below average, with an annual frequency of 8.2% (723.2 hours, Figure 2). Month-to-month variability is seen during the first half of the year with April and June being the most prolific months for the process; each month had ~150 hours of BLSN, easily falling outside the third quartile of the distributions. Observations of BLSN were above average for most of the first half of the year, followed by below-normal occurrence in the late winter and spring. For example, only 2.7 hours of BLSN were reported in November (Figure 2b).

3 AMF2 Observations of BLSN

3.1. AMF2 instrumentation

This article is protected by copyright. All rights reserved.

Accepted Article

A number of in situ observations were available at the AMF2 for the AWARE campaign. The facility had a variety of Vaisala instruments to measure basic meteorological properties (Ritsche & Prell, 2011). These measurements included barometric pressure (PTB330), temperature and relative humidity (HMP155), wind speed and wind direction (WS425), and a visibility, present weather and precipitation sensor (PWD22). Instruments were installed at standard AGL heights of 1 m (pressure), 2 m (temperature, relative humidity, present weather), and 10 m (wind). Visibility measurements are based on optical forward scattering leading to measurements with ± 5% uncertainty (Ritsche & Prell, 2011). The HMP155 measures temperature using a four-lead, platinum resistance thermometer, while the relative humidity is proportional to the capacitance from a polymer film (Ritsche & Prell, 2011). Finally, the WS425 uses ultrasonic measurements to retrieve wind properties (Ritsche & Prell, 2011).

Surface observations also included two instruments for precipitation: an optical rain gauge from Optical Scientific Inc. (ORG-815-DR) and the OTT Particle Size and Velocity disdrometer (Parsivel^2). The Parsivel^2 uses a 650 nm laser to project a 27 mm by 180 mm horizontal sheet of light onto the receiver, measuring the shadow of particles that pass through by the reduction in voltage received (OTT Hydromet, 2016). This allows for direct measurement of particle size and speed. The following variables are then derived: particle size spectrum, type and intensity of precipitation, kinetic energy, radar reflectivity, and horizontal visibility. In practice, particles from 0.25 to 25 mm in diameter can be measured by the instrument, sorted into 32 size classes of varying widths. The two size bins of smallest diameter (less than 0.25 mm) are not typically used due to low signal-to-noise ratio (Battaglia et al., 2010). Particle fall speeds are also sorted into 32 classes, with 0.2 and 25 m s^{-1} being the minimum and maximum detectable fall speeds, respectively (OTT HydroMet, 2016).

A suite of remote sensing instruments was also deployed at the AMF2. For this initial study, only the Vaisala CL31 ceilometer is discussed as it is the primary instrument used for the preexisting BLSN detection algorithm. The CL31 is a lidar system transmitting at a single wavelength (910 nm at 25°C), receiving the backscatter with an avalanche photodiode receiver (Morris, 2016). The CL31 yields data with 16 s samples and 10 m vertical grid spacing up to approximately 7.5 km above the instrument. ARM originally provided ceilometer data with 30m vertical averages. This data has since been reprocessed to the original 10 m spacing.

The ceilometer uses overlapping transmitting and receiving optics such that beam overlap occurs closer to the instrument than other lidars, producing data only 10 m above instrument level (Morris, 2016). The instrument includes a built-in algorithm to correct unrealistically high backscatter values in the first range bin due to window obstruction (Gossart et al., 2017). This filter introduces artifacts into the data in the first range bin, resulting in data that is consistently higher than that in the following bins. For this reason, the first range bin is not used in the BLSN detection algorithm. The ceilometer also uses relatively low energy (310 W), allowing for more economical operation (Morris, 2016). Since the energy of the emitted pulses is quite low, many pulses are averaged to reduce random background noise (Morris, 2016). The low emitted energy can introduce attenuation issues, particularly in mixed events where snow is both falling and blowing. While this is not expected to affect the retrieval of BLSN plume heights for cases under clear sky, it may cause issues in determining the depth of layers with more complicated hydrometeor profiles.

3.2. Gossart et al. (2017) BLSN detection algorithm

Gossart et al. (2017) developed an algorithm to detect BLSN from ceilometer attenuated backscatter profiles (referred to herein as the Gossart algorithm). Prior to running the algorithm, hourly running means were created from the original 16 s ceilometer profiles to smooth noise in the data, including laser-focusing issues that periodically appear in the 4th to 6th range bin. The algorithm is summarized in the following paragraphs. For additional details and reasoning behind the decisions made, readers are referred to Gossart et al. (2017).

The first step of the algorithm is to check whether backscatter in the lowest usable bin (bin 2, 10-20 m above the ceilometer) is higher than the clear sky threshold. The clear sky threshold is set by subjectively selecting periods of clear sky observed by the ceilometer and using the 95th percentile of the backscatter in the lowest usable bin. For the AMF2, this value was $21 \cdot 10^{-4}$ km^{-1} sr^{-1}, similar to the original values of 21- and $32.5 \cdot 10^{-4}$ km^{-1} sr^{-1} used for Princess Elisabeth and Neumayer III stations, respectively, in Gossart et al. (2017). The algorithm then looks for a decreasing profile by checking if backscatter in the lowest usable bin is higher than the average of the backscatter in the third to seventh bin (30-80 m). If these criteria are met, BLSN is detected and the algorithm ascends the profile, bin-by-bin, until the backscatter falls below the clear sky threshold (Category 1, clear sky BLSN) or begins to increase with height (Category 2, BLSN with clouds/precipitation). The exception for this strategy is for intense events with strong

This article is protected by copyright. All rights reserved.

backscatter due to both falling and/or blowing snow. If backscatter in the lowest usable range bin is > $1000 \cdot 10^{-4}$ km^{-1} sr^{-1}, the profile is labeled as an intense mixed event (Category 3).

In summary, the algorithm sorts profiles into four categories: non-BLSN, clear sky with BLSN (Category 1), cloud/precipitation with BLSN (Category 2), and intense mixed events (Category 3). Schematics showing the three BLSN categories are provided in Figure 4. The non-BLSN profiles are those that show no ground-based maximum in backscatter. The BLSN with cloud/precipitation and clear sky BLSN appear as profiles with high backscatter in the low levels with and without secondary peaks in backscatter at higher altitudes, respectively. Intense mixed events are those with very high backscatter in the low levels that can attenuate the ceilometer to various extents. Combined with existence of BLSN and falling snow, a variety of backscatter profiles can exist for this category, making the height of the BLSN more difficult to detect.

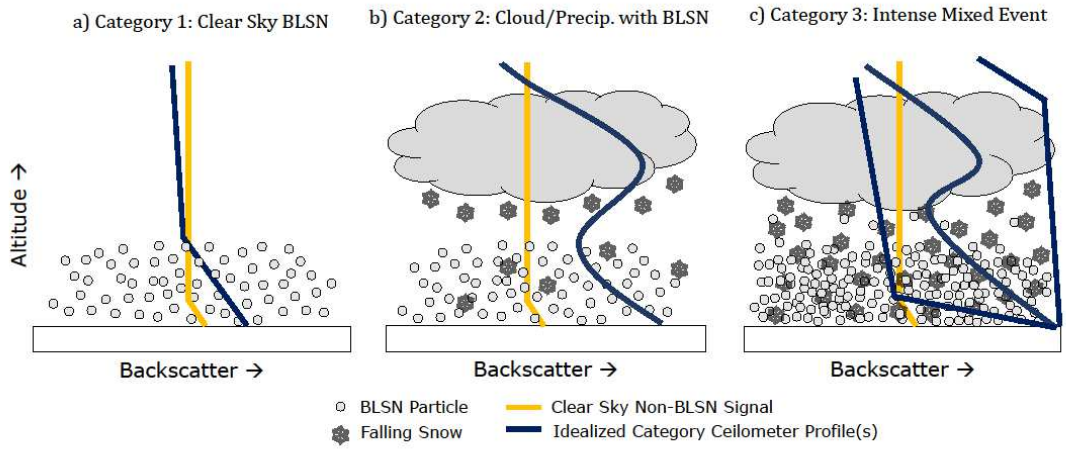

Figure 4. Diagrams of (a) clear sky BLSN, (b) clouds/precipitation with BLSN, and (c) intense mixed events. Orange and dark blue lines represent the clear sky signal and observed backscatter profiles from the ceilometer, respectively. Multiple profiles are shown for Category 3 to demonstrate how profiles vary by the amount of hydrometeors and resultant attenuation.

3.3. A revised BLSN detection algorithm

Based on performance of the original algorithm, manual inspection of cases, and the goal of eventually merging the ceilometer with additional radar and lidar datasets available with the AMF2, several additional modifications were made. First, manual inspection showed that the hourly running means (225 profiles) applied in the Gossart algorithm elongated the signal of some events, leading to a positive bias in frequency of detected BLSN (Figure S1). Time averaging was reduced to five-minute periods (18 profiles) as this is a common interval used with other profiling instruments at ARM sites (e.g. Clothiaux et al., 2000; Kennedy et al., 2014; Mace et al., 2006). Sensitivity tests demonstrated the varying of temporal averaging primarily impacted the results by a downward shift in frequency (see Section 3.4).

The second adjustment made to the algorithm was the inclusion of meteorological thresholds to increase confidence that BLSN was actively occurring at the AMF2. These included conservative thresholds of 10 km for visibility to ensure the backscatter signal was not decoupled from the surface layer, as the definition of BLSN requires visibility at 2 m to be reduced. A wind speed threshold of 3 m s^{-1} (Mellor 1965) was chosen to remove cases of stagnant fog. Fog appears similarly to BLSN in backscatter profiles alone, but the application of a wind speed threshold can rule out cases in which there are low-level scatterers present but insufficient wind to support BLSN. Modification of these thresholds resulted in minor differences in the detection of BLSN. For example, doubling the wind speed threshold to 6 m s^{-1} reduced total hours of BLSN by 7.1% while a reduction in visibility to 5 km led to a 7.8% relative change. Despite these thresholds, advection fog was still falsely detected by the algorithm during the summer months. Advection fog with moderate wind speeds is relatively common during the austral summer at McMurdo Station (Lazzara, 2008). In an effort to remedy this issue, an additional 90% relative humidity threshold was included to

This article is protected by copyright. All rights reserved.

separate fog from BLSN (Figure S2). While imperfect, this value offered the best balance of retaining nearly all of the BLSN signal throughout the year and reducing false positives during the summer months. Additional values were tested in 5% increments, but reductions led to BLSN being removed while increases did not sufficiently remove fog. The updated algorithm is referred to as the five-minute algorithm and versions are included with (5-min + MET) and without (5-min) thresholds in Section 3.4.

The three versions of the algorithm were compared to human observations to grossly assess performance. Although the human observations are not quite an apples-to-apples comparison, the comparison can provide insight into the potential skill of the algorithm (or human observers for that matter). To do this, output of the algorithms was grouped into the three-hour periods of the human observations for comparison. The algorithm output is converted to binary, to show whether BLSN has occurred within the period, rather than show specific categories. BLSN was said to be detected by an algorithm if at least 20 minutes of BLSN occurred within the period. Periods of BLSN shorter than 20 minutes are likely to go unreported by human observers. This is also the period used in the analysis performed in Gossart et al. (2017). The percent correct is calculated for each algorithm based on two-by-two contingency analysis based on the NOAA Forecast Verification Glossary. The percent correct (*PC*) describes the amount of agreement between the algorithm and the human observers and is calculated as

$$PC = \frac{A + D}{A + B + C + D} \times 100\% \quad (1)$$

where the variables are as defined in Table 1.

Table 1. 2x2 Contingency table for comparisons between human observations and algorithm results.

		Human	
		BLSN	Non-BLSN
Algorithm	BLSN	A	B
	Non-BLSN	C	D

3.4. Algorithm Results

3.4.1. Comparison to human observations

Monthly BLSN frequencies from the algorithms are shown in Figure 5a while seasonal and total values are listed in Table 2. For comparative purposes, human observations are also provided along with the frequencies of visibility measurements < 10 km. The algorithms have comparable seasonal cycles of BLSN with local maxima and minima during similar months. Of the methods analyzed, the Gossart algorithm had the highest positive bias compared to human observations with 1234.9 vs. 723.2 hours detected. In a relative sense, this difference was notably larger for the summer (DJF), with a ~500% increase over human observations. The 5-min + MET and 5-min algorithms detected 649.2 and 1044.8 hours of BLSN, respectively. The only month in which human observers reported a higher occurrence of BLSN than the algorithms was in April, which was also the peak month for human observations during the campaign.

Separation of BLSN events by category shed additional light on the process at McMurdo Station (Figure 5b). Like the 5-min + MET algorithm, all methods detected a higher frequency of intense mixed events (Category 3) than other categories. This means BLSN is closely tied to ongoing precipitation events at this location. Seasonally, this is most common during the autumn and early winter (March to June). Once snow accumulates at this location, clear sky BLSN becomes more likely until peaking during August. At this point, warming conditions reduce the likelihood of BLSN and frequencies drop for all categories into the summer.

The impacts of time averaging can be identified by comparing results between the Gossart and 5-min algorithms. Over the course of the year, the alteration of temporal averaging led to a decrease of BLSN detection from 1234.9 to 1044.8

This article is protected by copyright. All rights reserved.

hours (a 2.2% reduction in absolute frequency). Most of this change was seen when the averaging period was increased above 15 minutes (not shown). The difference between these two methods varied month-to-month shedding light on temporal variability in the ceilometer backscatter. These differences were largest during April, July, and August suggesting BLSN occurrence had spatial heterogeneity, such as what has been seen at other locations (Scarchilli et al., 2010; Kennedy & Jones, 2020). These differences were also greatest for Category 1 and 2 events (not shown). Manual inspection of ceilometer data supports this conclusion (Figure S1), but unfortunately, this time of year did not allow for the analysis of passively sensed satellite data as there was insufficient solar radiation to detect BLSN with near-infrared bands (Palm et al., 2011; Kennedy and Jones, 2020).

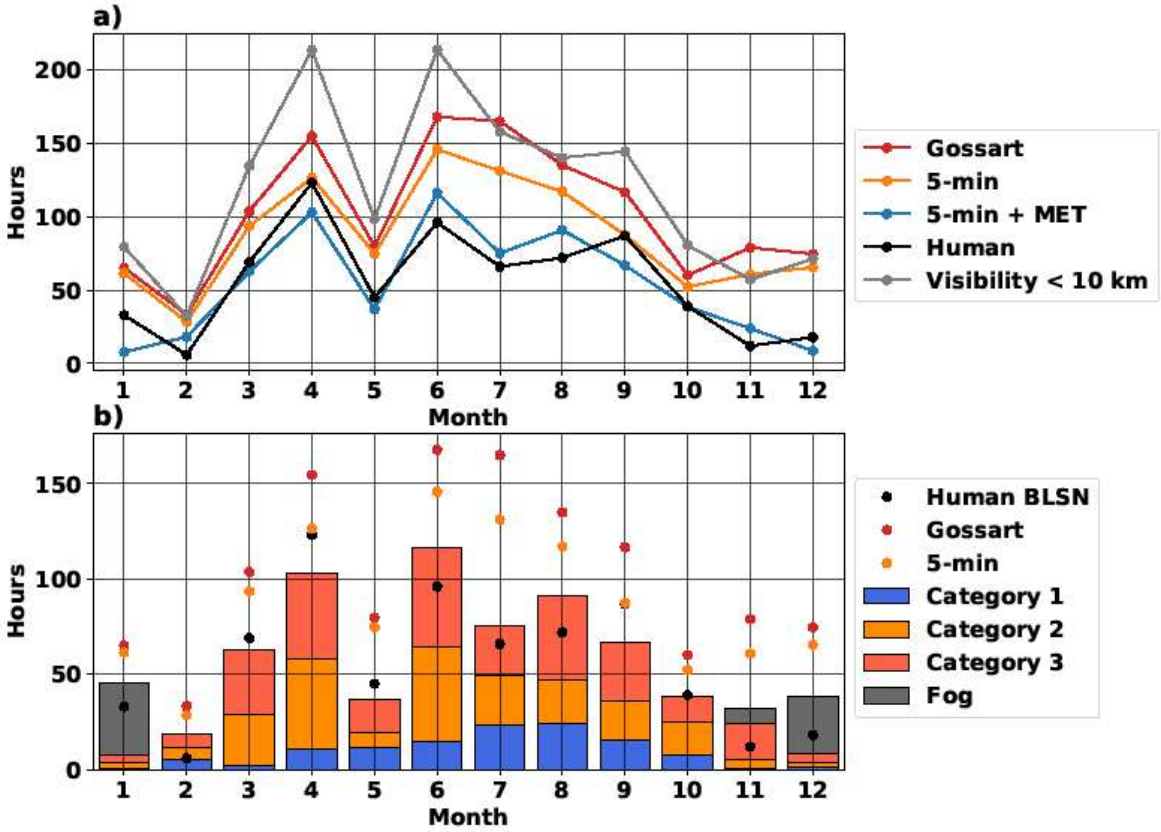

Figure 5. a) Monthly hours of BLSN detected by humans, ceilometer-based algorithms, and the visibility sensor during the 2016 AWARE campaign. b) Monthly hours of fog and BLSN separated by category detected by the 5-min + MET algorithm. For reference, select algorithms are shown with colored dots.

Inclusion of wind speed, visibility, and relative humidity thresholds had the largest impact on detection of BLSN. As this can be considered a quality-control or subsetting process that helps confirm BLSN is actively occurring at the surface, detection of the process is decreased year-round (Figure 5). In total, 649.2 hours were detected by the 5-min + MET algorithm (frequency of 7.4%), slightly below the results for human observations. When thresholds were added to the Gossart algorithm, the frequency was only ~36 hours above that of 5-min + MET, virtually negating the differences due to temporal averaging. Since the majority of the changes to the algorithm are due to these thresholds, the Gossart algorithm with thresholds can detect BLSN effectively, but the five-minute averaging periods allow for use with additional instrumentation to gain more insight into the plume properties and reduces the over-smoothing of shorter BLSN events.

Inspection of individual months revealed some notable differences in the results of the algorithms. During the month of April, the 5-min + MET algorithm had ~30% less hours of BLSN than the original Gossart algorithm and human observations. Half of this difference can be explained by the lack of temporal averaging. In this case, five-minute averages appeared to better handle artifacts in the lower bins of the ceilometer profiles that were more common in this month. The remainder was removed due to the wind speed threshold not being met. Other factors include April having the highest number of hours of observed falling snow, so complicated backscatter profiles were commonplace. This

This article is protected by copyright. All rights reserved.

led to cases where BLSN was observed but not detected by any algorithm. Further, several dates had human observations with continuous (+24hr) BLSN detection whereas visibility and ceilometer observations suggested BLSN was not continuous at the surface. It is hypothesized that some of this discrepancy may be due to periods of suspended blowing snow above the surface layer. An example of this is provided in Figure S1 (see 12:00 to 13:30 UTC).

Table 2. Seasonal and total BLSN hours and frequencies for each algorithm shown in Figure 5. The five-minute algorithm is further broken down into each category of BLSN.

Algorithm	BLSN Hours (Frequency)				
	Summer (DJF)	Autumn (MAM)	Winter (JJA)	Spring (SON)	Total
Human	36.7 (1.7%)	282.9 (12.8%)	307.4 (13.9%)	96.2 (4.4%)	723.2 (8.2%)
< 10 km visibility	175.6 (8.0%)	438.8 (19.9%)	503.8 (22.8%)	274.7 (12.6%)	1392.8 (15.9%)
Gossart	173.2 (7.9%)	338.2 (15.3%)	467.8 (21.2%)	255.7 (11.7%)	1234.9 (14.1%)
5-min	155.3 (7.1%)	294.8 (13.4%)	394.0 (17.8%)	200.6 (9.2%)	1044.8 (11.9%)
5-min+MET	34.8 (1.6%)	202.8 (9.2%)	282.1 (12.8%)	129.5 (5.9%)	649.2 (7.4%)
Category 1	7.0 (0.3%)	24.3 (1.1%)	63.2 (2.9%)	23.2 (1.1%)	117.7 (1.3%)
Category 2	11.3 (0.5%)	81.8 (3.7%)	98.1 (4.4%)	43.2 (2.0%)	234.3 (2.7%)
Category 3	16.5 (0.8%)	96.7 (4.4%)	120.8 (5.5%	63.2 (2.9%)7	297.1 (3.4%)

Another major difference caused by the inclusion of thresholds occurred during the summer months. The 5-min + MET algorithm performed notably better during this season due to the removal of fog cases. The most important contributor to this reduction was the inclusion of the relative humidity threshold. While imperfect (manual inspection of data noted missed cases in November), the chosen value (90%) prevented wintertime BLSN cases from being removed. Overall, it is concluded that the other algorithms are biased high by at least 5% from November – January (Figure 5b) although this can also be remedied by including MET thresholds to the Gossart algorithm.

Agreement between the algorithms and human observations varied seasonally (Figure 6). The average PC for the Gossart algorithm was 76.5%, which is similar to the results of Gossart et al. (2017), though monthly values were as low as 61.0% (seen in July). The 5-min + MET algorithm had the highest PC in all months, ranging from 75.5-94.7%. Notably, the PC was still highest for the 5-min + MET algorithm during April even though the total number of hours observed by humans was closest to the results of the Gossart algorithm. The 5-min algorithm had a PC that was slightly higher than the Gossart algorithm throughout the year, meaning that the periods of BLSN detected by the 5-min algorithm coincided with human observations more often than the Gossart algorithm. The PC is highest for all algorithms during the summer months (DJF). This is expected due to the lower frequency of BLSN allowing for correct null detections to dominate the statistic.

Another factor potentially affecting the seasonality of the agreement is shortcomings of the human observations, rather than failings of the algorithm. Human observations are inherently subjective; what one observer may denote as BLSN, another may not. The record is expected to be biased towards longer or more intense periods of BLSN, as the observer only records the number of hours of occurrence of a phenomena within a three-hour period. It is likely that some short-lived BLSN plumes may be missed, leading to discrepancies between the algorithm and the human. This is supported by the type of human observations made during three-hour periods with 5-min + MET BLSN detections (Figure 7). As intensity of events in both duration and category increases, the likelihood of humans identifying the process increases. Because this analysis does not include correct null events, the challenges of comparing the two types of BLSN detection is readily apparent; BLSN is identified simultaneously for only ~50% of the 3-hr periods, and this is reduced to ~40% for the Gossart algorithm (not shown).

Synthesizing this section, an annual range of BLSN can be estimated at McMurdo Station by using the range provided by the algorithms and human observations for the fall, winter and spring seasons, then relying on human observations and the final algorithm as guidance for the summer. During the 2016 AWARE campaign, this technique yields a modified frequency of 7.4-12.5%. Extrapolating this to the 2002-2018 period shown in Section 2, BLSN frequencies can range from 3.4-21.3% in any given year, with a mean BLSN of 8.0-14.0%. This is approximately 2-3 times higher than the values provided by space-borne lidar (4%, personal communication with Stephen Palm). This is expected

This article is protected by copyright. All rights reserved.

considering the aforementioned limitations of detection of BLSN in the presence of clouds. Provided that lower-end values are associated with simultaneous observations at the surface, these numbers should be thought of as periods of actively occurring blowing snow at the site while higher-end values may be more representative of regional BLSN occurrence as BLSN may become suspended above the surface layer. Regardless, modelers are cautioned that these values are only representative in the immediate vicinity of the station and frequencies for coarse grids may vary substantially given the known influences of topography in the region.

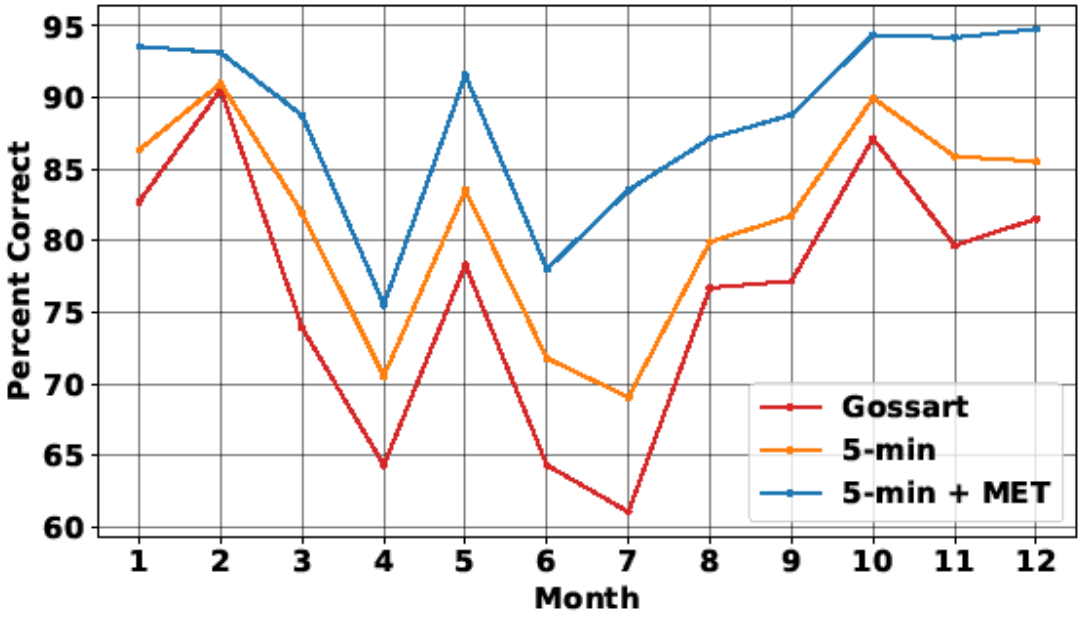

Figure 6. Percent correct by month for each algorithm compared to human observations during AWARE.

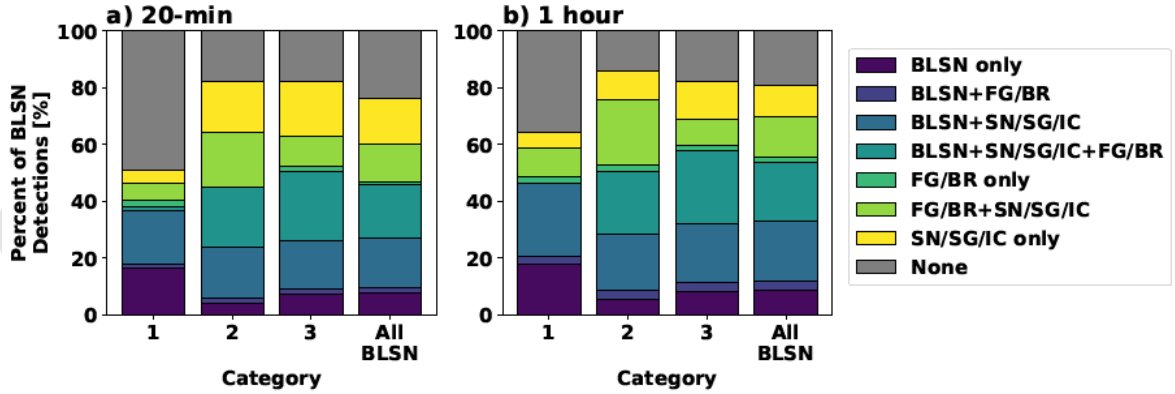

Figure 7. Category of human observations associated with 5-min + MET BLSN detections for a minimum of a) 20-min and b) 1-hr of algorithmic detections during each 3-hr human observation period.

3.4.2 Parsivel² measurements

Although the Parsivel² is only sensitive to particles ~250 μm and greater, it was hypothesized the instrument could provide enough information about the large tail of the BLSN particle size distribution (PSD) (e.g. Gordon & Taylor, 2009; Mellor, 1965; Nishimura & Nemoto, 2005), to distinguish between the categories of BLSN, falling snow, and fog. Distributions and mean particle counts were computed for the various categories (Figure 8). Mean particle counts are lowest (highest) for Category 1 (3) events while fog has significant overlap with all categories.

This article is protected by copyright. All rights reserved.

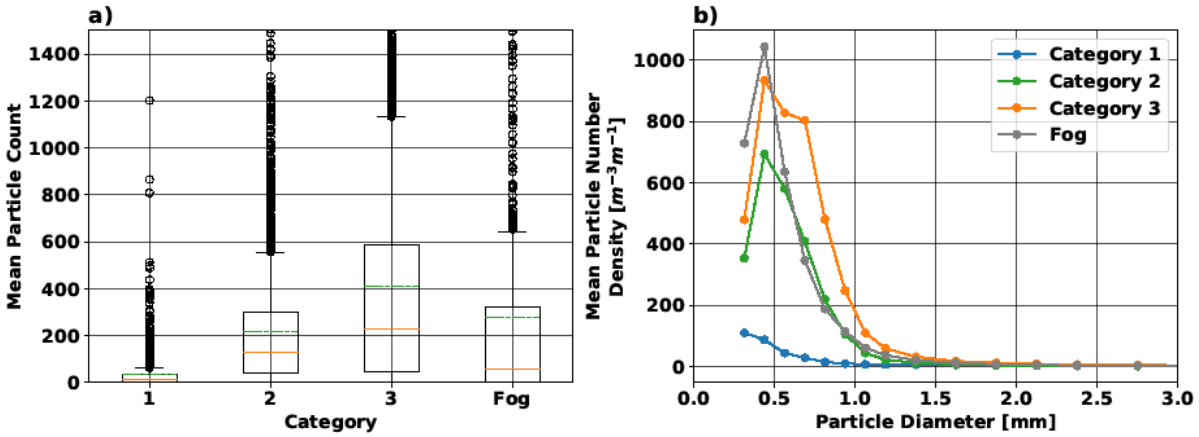

Figure 8. a) Boxplots of mean particle counts from the Parsivel² for each category based on the 5-min + MET algorithm. The orange solid and green dashed lines represent the median and mean of the distributions, respectively. b) Mean particle number density distributions from Parsivel² separated by category.

The mean PSDs for each category are shown in Figure 8b. For all categories, the peak occurs at particle sizes of 0.3-0.5 mm. Fog events have the highest peak particle number density, along with significant variation in mean particle counts. Category 3 events have a greater quantity of larger diameter particles which would be expected with intense mixed events including falling snow. Overall, Parsivel² particle counts and number densities alone do not appear to aid in separating scenes of hydrometeors.

Despite this finding, manual inspection of cases suggested there were some distinguishing differences between events (see Section 4). Provided characteristics and limitations of the Parsivel² have been documented for falling snow (Battaglia et al., 2010) but minimally for BLSN (Maahn 2010 noted a positive bias for precipitation rate during BLSN events), further investigation was warranted. Given the importance of wind for the process, Parsivel² observations during time periods of detected BLSN were segregated by wind speed for all events (Figure 9). An immediate relationship is seen between wind speed and PSD. As wind speed increases above a threshold of ~10 m s^{-1}, the shape of the PSD changes markedly with number density increasing at diameters greater than 1mm. This comes at the expense of a decrease in smaller particles. While larger aggregate snowflakes can occur at coastal locations in Antarctica (Konishi et al., 1992; Souverijns et al., 2017), this signal occurs for all categories of BLSN including events with clear sky or a lack of fall streaks indicative of significant snowfall. To test whether this could be an artifact of instrument siting at the AMF2, a similar analysis was performed for Parsivel² observations from the Phoenix Airfield Antarctica Precipitation Site (APS) deployed during 2019 and a local field campaign in North Dakota that sampled several blizzard events in 2020. This artifact was present at these sites in varying extents, suggesting that the issue is most likely a fundamental limitation of the Parsivel². It is currently hypothesized that high number concentrations of BLSN may contribute to separate particles creating voltage signals indicative of singular particles with a greater diameter than reality. As a result, it is concluded Parsivel² observations should be used with caution during periods of wind greater than 10 m s^{-1}.

3.4.3. Environmental conditions during BLSN

To investigate the relationship between meteorological properties and BLSN occurrence, two-dimensional histograms were produced (Figure 10). Segregation by BLSN category are included within Figures S3 and S4. The results shown are for the 5-min algorithm, with the region satisfying 5-min + MET thresholds indicated by the area within (a-b) and above (c-d) the dashed lines. The Gossart algorithm produced nearly identical patterns to those of the 5-min algorithms (not shown).

This article is protected by copyright. All rights reserved.

Accepted Article

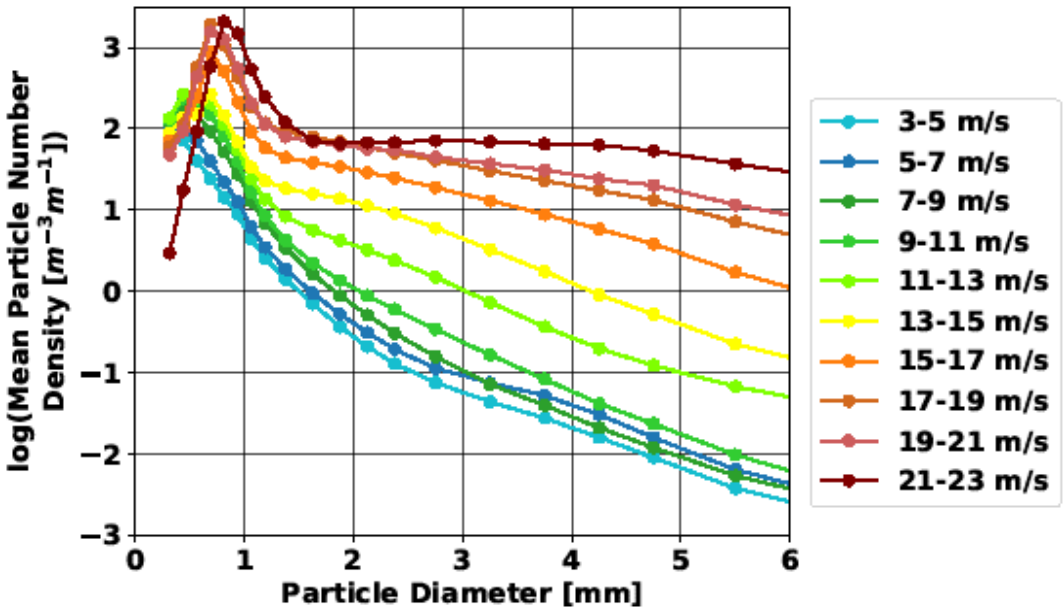

Figure 9. Logarithmic particle number density distributions from the Parsivel² segregated by wind speed increments during all BLSN events detected by the 5-min + MET algorithm.

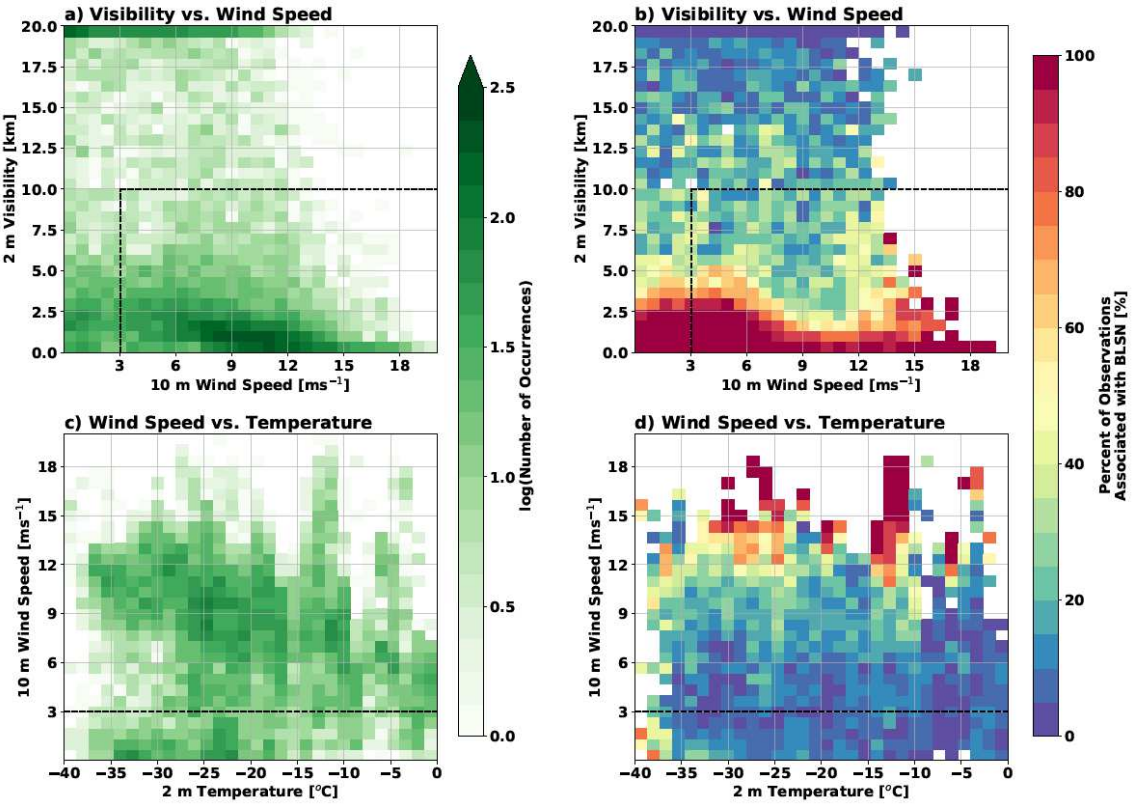

Figure 10. Two-dimensional histograms of 2 m visibility versus 10 m wind speed (a-b), and wind speed versus temperature (c-d) for all BLSN detections by the 5-min algorithm. The logarithmic number of occurrences of BLSN detected by the 5-min algorithm in each bin is shown in a and c, while the percent of observations in each bin associated with detected BLSN is shown in b and d. The dashed lines indicate the subset meeting the thresholds of the 5-min + MET algorithm.

This article is protected by copyright. All rights reserved.

First, the relationship between visibility and wind speed is investigated (Figure 10a-b). The majority of detections of BLSN occurred with 10 m wind speeds of 7.5-12.5 m s^{-1} and 2 m visibility of less than 3 km. Observations of very high wind speeds were uncommon, therefore there were few BLSN detections above ~17.5 m s^{-1}. Overall, low to moderate wind speeds (3-12.5 m s^{-1}) were associated with variable visibility observations (0-10 km), while BLSN with higher wind speeds tended to occur with visibility < 3 km. As category increases, visibilities decrease for equivalent wind speeds (Figure S3). Human observations and BLSN associated with Category 1 events were likely at wind speeds > 6 m s^{-1}. This is consistent with the probability of BLSN and decreased visibility increasing with falling precipitation at lower wind speeds. It also suggests that wind thresholds could be increased for clear sky blowing snow events.

The subset of data with MET thresholds applied removed a peak of detections associated with no reduction in surface visibility, as well as a local maxima at wind speeds < 2 m s^{-1}. Few human observations occur outside of this region for Category 1 and 2 events further supporting thresholding (Figure S3). The percent of observations associated with BLSN increased as visibility decreased, regardless of the wind speed. Most of this result is due to the inclusion of precipitating events within Categories 2 and 3.

Figure 10c-d shows the connection observed between wind speed and temperature. Detected BLSN occurred over a wide range of temperatures with no clear relationship seen. Separation by results by BLSN category yielded no additional insight other than allowing individual events to appear (Figure S4). The likelihood of BLSN increased as the wind speeds increased at all temperatures, agreeing with previous studies. Finally, the conservative wind speed threshold removed a cluster of cases at cold temperatures (< -30□C) and low wind speeds (< 1 m s^{-1}) that may be associated with ice fog/diamond dust.

Provided the complexity of terrain in the region, BLSN was also investigated by wind direction. Complex wind roses are seen (Figure 11). The most frequent wind direction observed at McMurdo Station during AWARE was northeasterly with over half of the wind observations coming from this quadrant (Figure 11a). This is likely due to topographic effects, as McMurdo Station is bounded by the Transantarctic Mountains to the west and south and Mount Erebus to the north (Costanza et al., 2016). This is also the most common wind direction for all BLSN categories due to its frequent occurrence, shown in Figure 11b-d. Fog detections were found at similar wind directions to that of Category 1 (not shown).

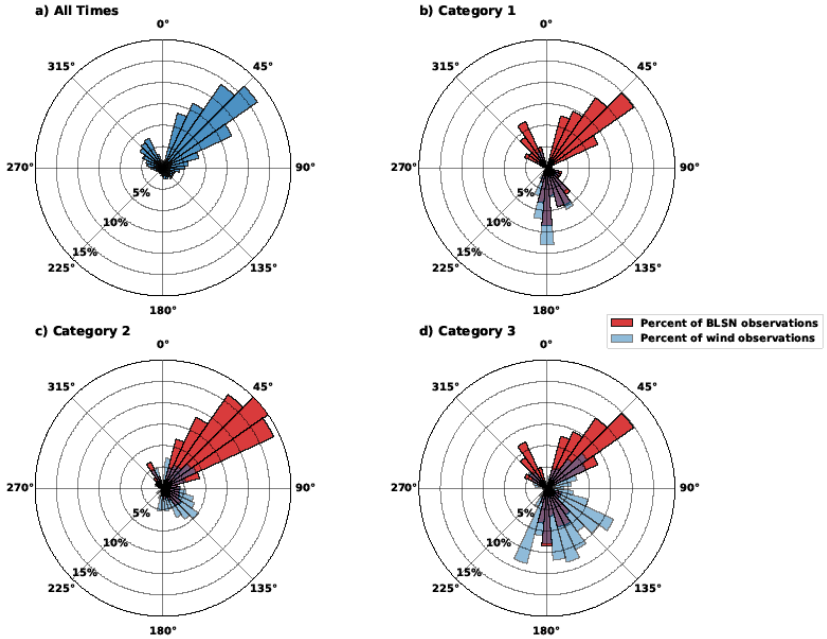

Figure 11. Distribution of 10 m wind direction occurrence for each five-minute period during 2016 for a) all times and b-d) Category 1-3 BLSN cases detected by the 5-min + MET algorithm. Blue (red) bars represent the percent of wind (BLSN) observations in each 10° wind direction bin.

This article is protected by copyright. All rights reserved.

Accepted Article

Although southerly winds are relatively uncommon at McMurdo Station, they are associated with BLSN a higher proportion of the time. This is particularly true for intense mixed events; over 10% of wind observations coming from 170-190° are associated with Category 3 events. This pattern is evident in the other BLSN categories to a lesser degree. Strong wind events (> 15 m s^{-1}) observed at McMurdo Station often occur with southerly winds associated with a deep low pressure system approaching the region from the north (Seefeldt et al., 2003; Weber et al., 2016) meaning that it may be more likely to see more intense BLSN events during the occurrence of these southerly winds.

4 Example Case Studies

To demonstrate properties of the 5-min + MET algorithm, two case studies are presented that represent the variety of BLSN events McMurdo station receives.

4.1 Clear sky BLSN: 4-5 July 2016

From 2200 UTC 4 July 2016 to 0600 UTC 5 July 2016, a BLSN event was observed by both human observers and the ceilometer-based algorithms (Figure 12). Human observers noted snow during the event, but this is not supported in the backscatter profiles at the AMF2. Analysis of vertically pointing radar data revealed surface-based backscatter decoupled from cirrus clouds at heights above 4 km AGL (not shown). In other words, this BLSN event was independent of falling precipitation. Initial detection of BLSN by the AMF2 around 2200-2300 UTC was tied to rapid fluctuations in wind speed and direction suggesting the influence of topography. The high Parsivel^2 particle counts around 2300 UTC for example, were associated with north-easterly winds shifting to northwesterly before shifting back by 2345 UTC (Figure 12c-d). Backscatter profiles after this time led to straight forward detection of the blowing snow layer which had heights that reached up to ~200 m (Figure 12b). Modulation of the BLSN layer can be attributed to a change in wind intensity. During the most prolonged portion of the event (0000-0230 UTC), increasing heights can be seen as wind speed increased up to 17 m s^{-1}. Eventually, backscatter became intense enough to classify the BLSN as an intense mixed case (Category 3), although this is clearly not the case. As the winds began to subside by 0200 UTC (Figure 12d), plume heights dropped below the top of the backscatter column. This is caused by the backscatter increasing above the surface layer, suggesting that as the event waned, BLSN became suspended above the surface layer.

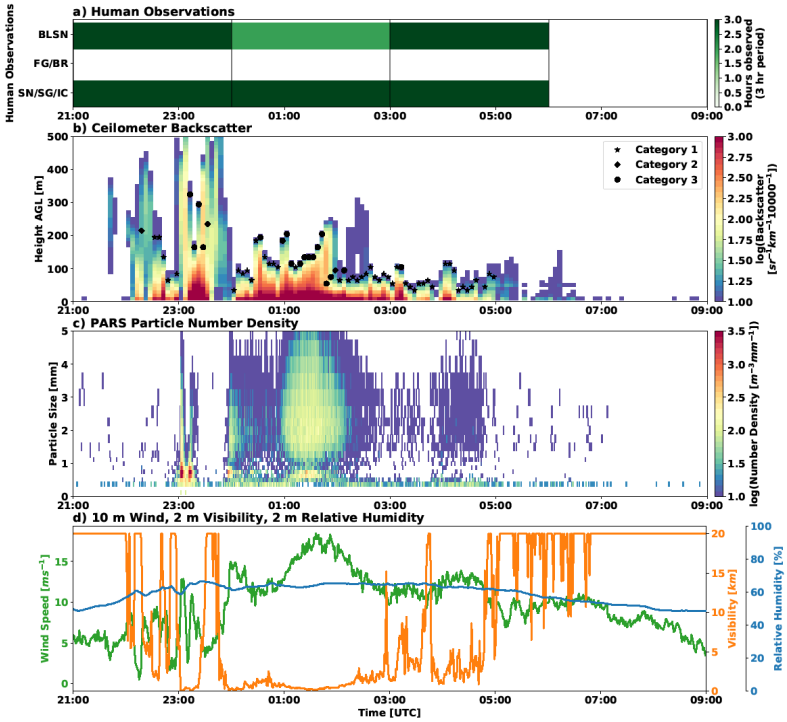

Figure 12. a) Human observations, b) five-minute average ceilometer attenuated backscatter, c) five-minute average Parsivel^2 particle number density, and d) five-minute average wind speed (green), visibility (orange), and relative humidity (blue) from MET instrumentation on 4-5 July 2016 at McMurdo Station. BLSN tops derived from the 5-min + MET algorithm are denoted by stars, diamonds, and dots for categories 1-3, respectively.

This article is protected by copyright. All rights reserved.

Accepted Article

This case exemplifies the limitations of the Parsivel[2] in high wind environments noted in Section 3.4.3. Particle number density peaks in the smallest particle sizes with a moderate number of larger particles with diameters of 2-5 mm. The periods of highest wind speeds are associated with broad increases in large particles detected. At around 0300 UTC, the BLSN becomes more variable, shown through the oscillating visibility observations and periodic ground-based peaks in backscatter. It is possible that the BLSN organized into horizontal convective rolls at this time (e.g. Kennedy et al. 2020), but without satellite imagery, this is purely speculative.

4.2. Intense mixed event: 12 June 2016

An intense mixed event occurred at McMurdo Station on 12 June 2016, lasting from approximately 0400 to 2300 UTC. This event saw falling snow and BLSN throughout its duration (Figure 13). The onset of the event is seen clearly in the visibility observations and is associated with increasing wind speed and low-level backscatter beginning around 0300 UTC. Unlike the previous case, there is backscatter extending above identified layers of BLSN. Further investigation of other radar and lidars demonstrated that ceilometer observations did not penetrate through the entire column of hydrometeors (Figure 14). From 0800 UTC onward, reflectivity was noted up to 5km AGL (Figure 14b).

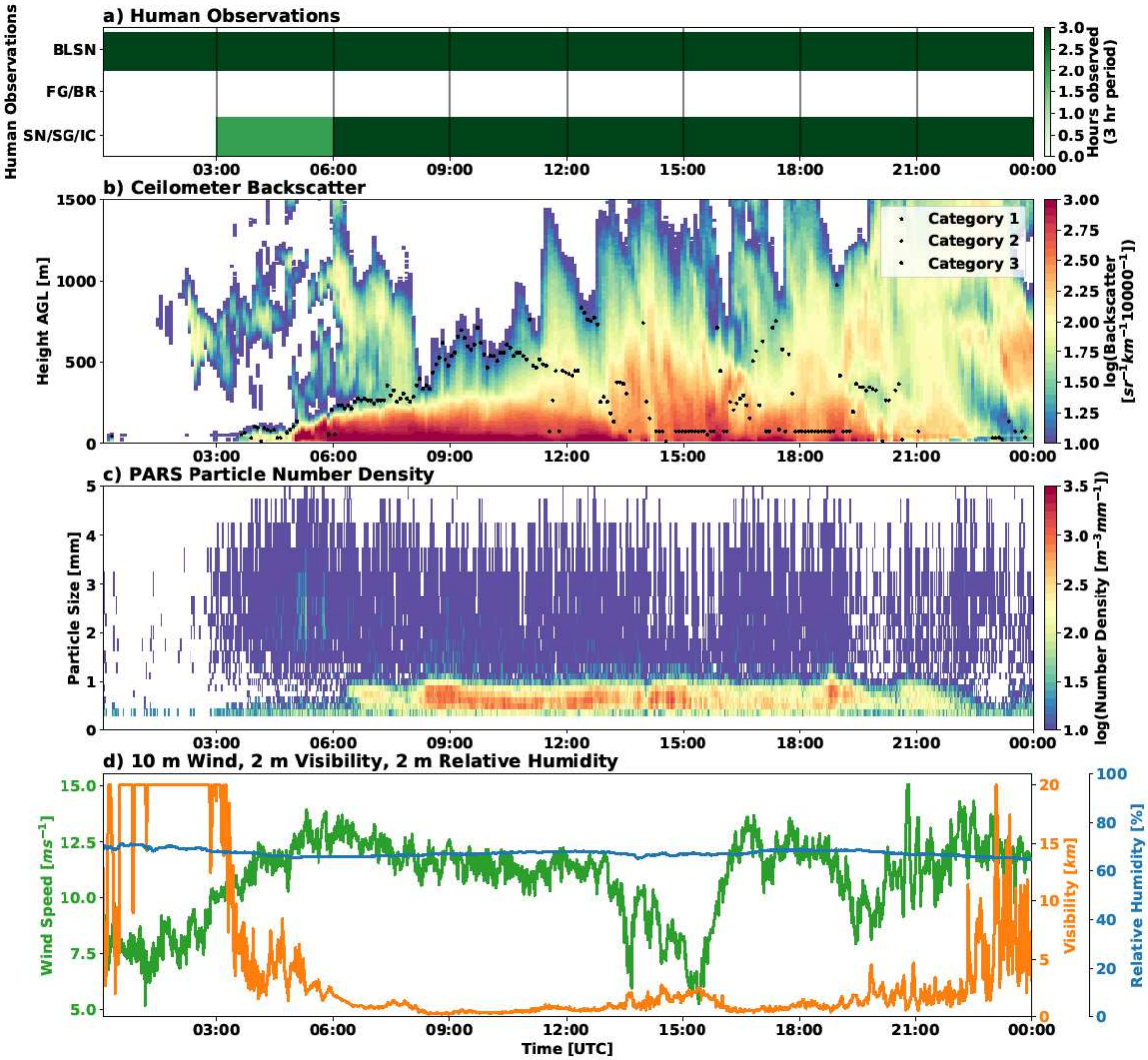

Figure 13. As in Figure 12, but for 12 June 2016.

Differences are also noted in Parsivel[2] particle number densities. While values increase in the smallest size bins first, time periods of falling and blowing snow are associated with a higher density of particles from 0.5 to 1 mm. Particle

This article is protected by copyright. All rights reserved.

Accepted Article

counts are also significantly higher than those seen in the clear sky event shown in the previous section. While some larger size particles are detected by the instrument, a clear bimodal distribution is not seen as in the previous case. The only hint of this artificial distribution occurs around 0600 UTC which also happens to be a local maximum for wind speed at 13 m s^{-1}.

The algorithm appropriately detects the presence of BLSN, but there are periods when the detected BLSN plume height is inconsistent. For example, heights from 0700-1300 UTC fluctuate depending on the presence and intensity of fall streaks modifying the column of ceilometer backscatter (Figures 13-14). Given this property and the frequency of intense mixed (Category 3) events at this location, statistics on BLSN plume heights are not presented herein. Rather, a multi-instrument algorithm is currently being developed with the inclusion of the other remote sensing platforms like the HSRL and KAZR (Figure 14). For example, several demarcations are visible during this event. HSRL backscatter (Figure 14a) has a strong gradient at a height of ~300m consistent with earlier detections from the ceilometer. Further, this region is associated with depressed values of both linear depolarization ratio (Figure 14c) and color ratio (Figure 13d). Physically this should make sense as the transition from the falling to blowing snow will involve changes in the PSD (shift to smaller diameter particles), and crystal habit (to irregular shapes). Changes in habit will influence the depolarization ratio (Sassen, 1991), while the color ratio serves as a proxy for particle size (Bourdages et al., 2009).

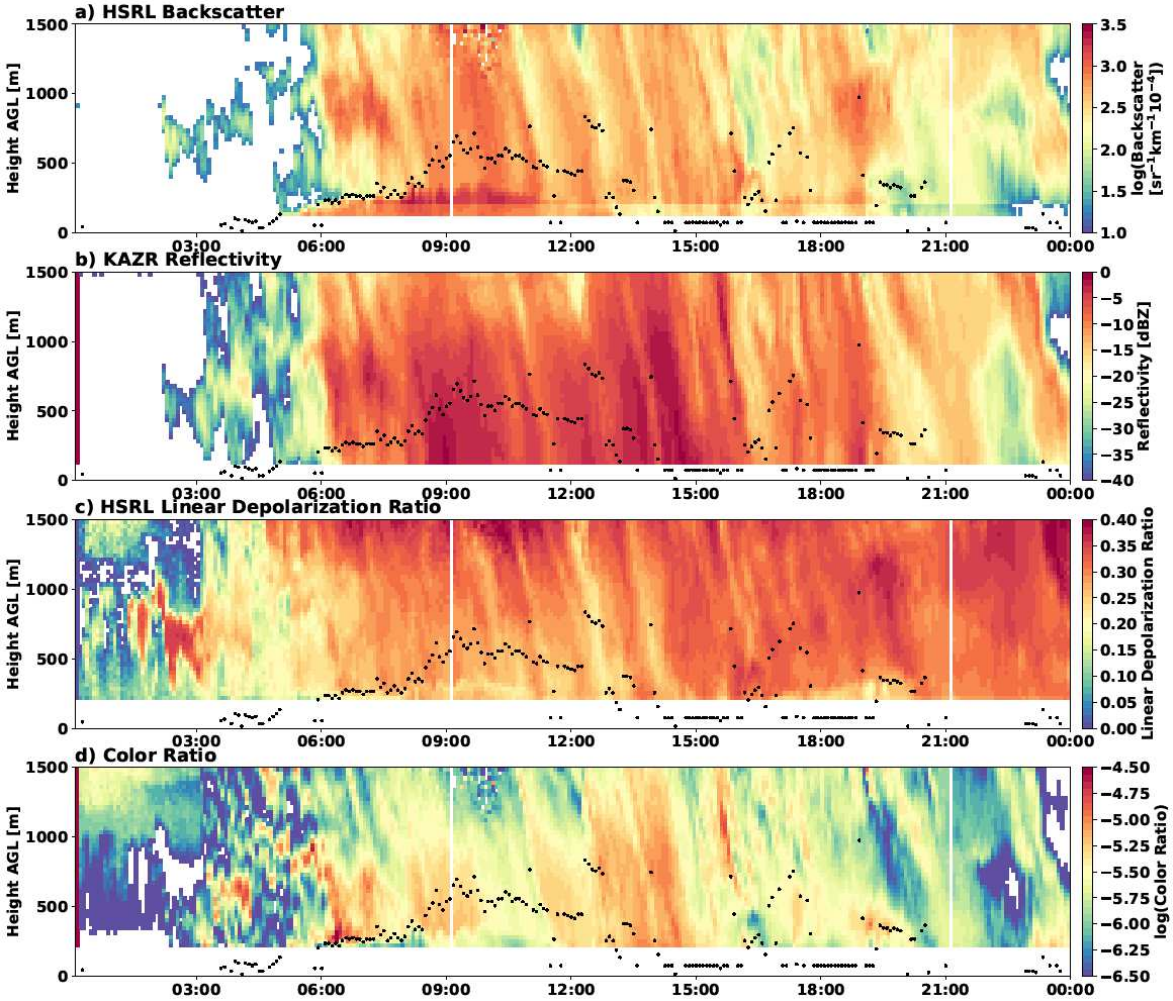

Figure 14. Five-minute average profiles of a) High Spectral Resolution Lidar (HSRL) attenuated backscatter, b) Ka-Band ARM Zenith Radar (KAZR) reflectivity, d) HSRL linear depolarization, and e) color ratio calculated as the ratio between KAZR reflectivity and HSRL backscatter on 12 June 2016. BLSN heights from the 5-min + MET algorithm are denoted with black dots.

This article is protected by copyright. All rights reserved.

Accepted Article

5 Conclusions

The presented climatology of human observations at McMurdo Station showed that annual BLSN frequency ranges from 4-14%. The majority of these observations occur concurrently with precipitation rather than on its own, and BLSN is most likely from April to October. Complex topography in the region complicates the process, and this may provide reasoning to the differences seen between the varying algorithms and instrumentation.

Ground-based in situ and remote sensing observations from the 2016 AWARE Campaign have been analyzed to assess the occurrence of BLSN at McMurdo Station. The ceilometer-based detection algorithm derived by Gossart et al. (2017) was applied to data from AWARE and its performance was found to be similar to the result when applied in Eastern Antarctica, though it had a large positive bias when compared to human observations (1234.9 vs. 723.2 hours). The addition of wind speed, visibility, and relative humidity thresholds and averaging to a five-minute temporal resolution led to increased agreement with human observations. The largest increases in agreement with human observations occurred in the austral summer months because of the removal of fog events by the applied relative humidity threshold. Since there is no ground truth due to the lack of reliable microphysical observations, it is impossible to determine the true accuracy of each method. Based on the algorithm results and human observations, it is estimated that the frequency of BLSN during AWARE was 7.4-12.5%. An average annual BLSN frequency of 8.0-14.0%, with a total range of 3.4-21.3%, is estimated for McMurdo Station. This is approximately 2-3 times higher than a previous satellite-based climatology (Palm et al., 2018), which was expected to be low due to the common presence of low cloud cover. Lower values are more likely to be associated with the process of BLSN actively occurring at the station while higher values may be more representative of the region due to the presence of the process above the surface layer or influences of topography.

The detection of BLSN by the algorithm is considered to perform quite well, but significant uncertainty is associated with the detected depth of the BLSN layer, particularly during intense mixed events. Overall, there is confidence in the detection of heights with Category 1 events, but ambiguous backscatter profiles when precipitation is occurring makes depth detection more complex for Category 2 and 3 events. Better understanding of plume depth is important to allow for more accurate estimations of impacts on the radiation budget, mass transport, and effects on regional surface mass balance. The new 5-min + MET algorithm will permit use of the suite of remote sensing observations available during AWARE to help refine the BLSN layer height. Lastly, the 5-min + MET algorithm may be applied to other ARM sites to gain a widespread understanding of the occurrence of BLSN. Assessment of BLSN plume heights and modeling of the process at McMurdo Station are the subject of future efforts.

Acknowledgments

This research is funded by DOE ASR grant DE-SC0019392. We would like to thank Michael Ritsche and his colleagues at ARM for reprocessing the ceilometer data, Alexandra Gossart for assistance with the ceilometer BLSN detection algorithm, the Antarctic Meteorological Research Center (AMRC) and the McMurdo Station Meteorology Office for the human observation data, Mark Seefeldt for sharing Parsivel^2 data from the Phoenix site, and the lidar group at the University of Wisconsin-Madison for providing the high-resolution HSRL data shown in Figure 14. Finally, we would like to Alexendra Gossart and one anonymous reviewer who provided a number of helpful comments that improved the analysis and clarity of the manuscript.

Open Research Statement

AMRC (human observation) data are available from at https://minds.wisconsin.edu/handle/1793/79355. ARM datastreams used for this study are available at the following locations: http://dx.doi.org/10.5439/1025220 (surface meteorology), http://dx.doi.org/10.5439/1498731 (Parsivel^2), and http://dx.doi.org/10.5439/1181954 (ceilometer).

References

Adhikari, L., Wang, Z., & Deng, M. (2012). Seasonal variations of Antarctic clouds observed by CloudSat and CALIPSO satellites. *Journal of Geophysical Research: Atmospheres*, *117*(D4). https://doi.org/10.1029/2011JD016719

This article is protected by copyright. All rights reserved.

Accepted Article

Agosta, C., Amory, C., Kittel, C., Orsi, A., Favier, V., & Gallée, H. (2019). Estimation of the Antarctic surface mass balance using the regional climate model MAR (1979–2015) and identification of dominant processes. *The Cryosphere*, 16.

Battaglia, A., Rustemeier, E., Tokay, A., Blahak, U., & Simmer, C. (2010). PARSIVEL Snow Observations: A Critical Assessment. *Journal of Atmospheric and Oceanic Technology*, *27*(2), 333–344. https://doi.org/10.1175/2009JTECHA1332.1

Bintanja, R. (2001). Modification of the wind speed profile caused by snowdrift: Results from observations. *Quarterly Journal of the Royal Meteorological Society*, *127*(577), 2417–2434. https://doi.org/10.1002/qj.49712757712

Bintanja, R., & Reijmer, C. H. (2001). A simple parameterization for snowdrift sublimation over Antarctic snow surfaces. *Journal of Geophysical Research: Atmospheres*, *106*(D23), 31739–31748. https://doi.org/10.1029/2000JD000107

Bourdages, L., Duck, T. J., Lesins, G., Drummond, J. R., & Eloranta, E. W. (2009). Physical properties of High Arctic tropospheric particles during winter. *Atmospheric Chemistry and Physics*, *9*(2), 7781–7823.

Budd, W. F. (1966). The Drifting of Nonuniform Snow Particles. In *Studies in Antarctic Meteorology* (pp. 59–70). American Geophysical Union (AGU). https://doi.org/10.1029/AR009p0059

Clothiaux, E. E., Ackerman, T. P., Mace, G. G., Moran, K. P., Marchand, R. T., Miller, M. A., & Martner, B. E. (2000). Objective Determination of Cloud Heights and Radar Reflectivities Using a Combination of Active Remote Sensors at the ARM CART Sites. *Journal of Applied Meteorology*, *39*(5), 645–665. https://doi.org/10.1175/1520-0450(2000)039<0645:ODOCHA>2.0.CO;2

Costanza, C. A., Lazzara, M. A., Keller, L. M., & Cassano, J. J. (2016). The surface climatology of the Ross Ice Shelf Antarctica. *International Journal of Climatology*, *36*(15), 4929–4941. https://doi.org/10.1002/joc.4681

Déry, S. J., & Yau, M. K. (2002). Large-scale mass balance effects of blowing snow and surface sublimation. *Journal of Geophysical Research: Atmospheres*, *107*(D23), ACL 8-1-ACL 8-17. https://doi.org/10.1029/2001JD001251

Elevant, K. (2010). COLLABORATIVE OBSERVATIONS OF WEATHER - A Weather Information Sharers' Community of Practice: In *Proceedings of the 6th International Conference on Web Information Systems and Technology* (pp. 392–399). Valencia, Spain: SciTePress - Science and and Technology Publications. https://doi.org/10.5220/0002810203920399

This article is protected by copyright. All rights reserved.

Accepted Article

Gallée, H., Guyomarc'h, G., & Brun, E. (2001). Impact of Snow Drift on the Antarctic Ice Sheet Surface Mass Balance: Possible Sensitivity to Snow-Surface Properties. *Boundary-Layer Meteorology*, *99*(1), 1–19. https://doi.org/10.1023/A:1018776422809

Gordon, M., & Taylor, P. A. (2009). Measurements of blowing snow, Part I: Particle shape, size distribution, velocity, and number flux at Churchill, Manitoba, Canada. *Cold Regions Science and Technology*, *55*(1), 63–74. https://doi.org/10.1016/j.coldregions.2008.05.001

Gossart, A., Souverijns, N., Gorodetskaya, I. V., Lhermitte, S., Lenaerts, J. T. M., Schween, J. H., et al. (2017). Blowing snow detection from ground-based ceilometers: application to East Antarctica. *The Cryosphere*, *11*(6), 2755–2772. https://doi.org/10.5194/tc-11-2755-2017

Gossart, A., Palm, S. P., Souverijns, N., Lenaerts, J. T. M., Gorodetskaya, I. V., Lhermitte, S., & van Lipzig, N. P. M. (2020). Importance of Blowing Snow During Cloudy Conditions in East Antarctica: Comparison of Ground-Based and Space-Borne Retrievals Over Ice-Shelf and Mountain Regions. *Frontiers in Earth Science*, *8*, 240. https://doi.org/10.3389/feart.2020.00240

Hanesiak, J. M., & Wang, X. L. (2005). Adverse-Weather Trends in the Canadian Arctic. *Journal of Climate*, *18*(16), 3140–3156. https://doi.org/10.1175/JCLI3505.1

Kennedy, A., & Jones, C. (2020). GOES-16 Observations of Blowing Snow in Horizontal Convective Rolls on 24 February 2019. *Monthly Weather Review*, *148*(4), 1737–1750. https://doi.org/10.1175/MWR-D-19-0354.1

Kennedy, A. D., Dong, X., & Xi, B. (2014). Cloud fraction at the ARM SGP site. *Theoretical and Applied Climatology*, *115*(1), 91–105. https://doi.org/10.1007/s00704-013-0853-9

Konishi, H., Muramoto, K., Shiina, T., Endoh, T., & Kitano, K. (1992). Z-R RELATION FOR GRAUPELS AND AGGREGATES OBSERVED AT SYOWA STATION, ANTARCTICA. *Proceedings of the NIPR Symposium on Polar Meteorology and Glaciology*, *5*, 97–103.

Lazzara, M. A. (2008). *A Diagnostic Study of Antarctic Fog* (Dissertation). University of Wisconsin-Madison, Madison, Wisconsin. Retrieved from https://www.aos.wisc.edu/aosjournal/Volume6/theses/Matthew_Lazzara_PhD_Thesis.pdf

Lenaerts, J. T. M., van den Broeke, M. R., Déry, S. J., König-Langlo, G., Ettema, J., & Munneke, P. K. (2010). Modelling snowdrift sublimation on an Antarctic ice shelf. *The Cryosphere*, *4*(2), 179–190. https://doi.org/10.5194/tc-4-179-2010

This article is protected by copyright. All rights reserved.

Accepted Article

Leonard, K. C., Tremblay, L.-B., Thom, J. E., & MacAyeal, D. R. (2012). Drifting snow threshold measurements near McMurdo station, Antarctica: A sensor comparison study. *Cold Regions Science and Technology*, *70*, 71–80. https://doi.org/10.1016/j.coldregions.2011.08.001

Li, L., & Pomeroy, J. W. (1997). Probability of occurrence of blowing snow. *Journal of Geophysical Research: Atmospheres*, *102*(D18), 21955–21964. https://doi.org/10.1029/97JD01522

Listowski, C., Delanoë, J., Kirchgaessner, A., Lachlan-Cope, T., & King, J. (2019). Antarctic clouds, supercooled liquid water and mixed phase, investigated with DARDAR: geographical and seasonal variations. *Atmospheric Chemistry and Physics*, *19*(10), 6771–6808. https://doi.org/10.5194/acp-19-6771-2019

Lubin, D, Verlinde, J., Bromwich, D., Vogelmann, A., & Russell, L. (2015). *ARM West Antarctic Radiation Experiment (AWARE) Science Plan* (No. DOE/SC-ARM-15-040) (p. 20). Retrieved from https://www.arm.gov/publications/programdocs/doe-sc-arm-15-040.pdf

Lubin, Dan, Zhang, D., Silber, I., Scott, R. C., Kalogeras, P., Battaglia, A., et al. (2020). AWARE: The Atmospheric Radiation Measurement (ARM) West Antarctic Radiation Experiment. *Bulletin of the American Meteorological Society*, *101*(7), E1069–E1091. https://doi.org/10.1175/BAMS-D-18-0278.1

Mace, G. G., Benson, S., Sonntag, K. L., Kato, S., Min, Q., Minnis, P., et al. (2006). Cloud radiative forcing at the Atmospheric Radiation Measurement Program Climate Research Facility: 1. Technique, validation, and comparison to satellite-derived diagnostic quantities. *Journal of Geophysical Research: Atmospheres*, *111*(D11). https://doi.org/10.1029/2005JD005921

Mahesh, A., Eager, R., Campbell, J. R., & Spinhirne, J. D. (2003). Observations of blowing snow at the South Pole. *Journal of Geophysical Research: Atmospheres*, *108*(D22). https://doi.org/10.1029/2002JD003327

Mellor, M. (1965). *Blowing Snow* (Cold Regions Research and Engineering Laboratory No. 3 sect. A3c). Hanover, New Hampsire. Retrieved from http://hdl.handle.net/11681/2625

Morris, V. R. (2016). *Ceilometer Instrument Handbook* (No. DOE/SC-ARM-TR-020) (p. 26). https://doi.org/10.2172/1036530

Nishimura, K., & Nemoto, M. (2005). Blowing snow at Mizuho station, Antarctica. *Philosophical Transactions of the Royal Society A: Mathematical, Physical and Engineering Sciences*, *363*(1832), 1647–1662. https://doi.org/10.1098/rsta.2005.1599

This article is protected by copyright. All rights reserved.

Accepted Article

NOAA. (1998, May). Training Guide in Surface Weather Observations. Retrieved June 27, 2019, from https://www.weather.gov/media/surface/SFCTraining.pdf

OTT HydroMet. (2016). *Operating instructions Present Weather Sensor OTT Parsivel2* (No. 70.210.001.B.E 12-1016). Retrieved from https://www.ott.com/download/operating-instructions-present-weather-sensor-ott-parsivel2-without-screen-heating/

Palm, S. P., Yang, Y., Spinhirne, J. D., & Marshak, A. (2011). Satellite remote sensing of blowing snow properties over Antarctica. *Journal of Geophysical Research: Atmospheres*, *116*(D16). https://doi.org/10.1029/2011JD015828

Palm, S. P., Kayetha, V., Yang, Y., & Pauly, R. (2017). Blowing snow sublimation and transport over Antarctica from 11 years of CALIPSO observations. *The Cryosphere*, *11*(6), 2555–2569. https://doi.org/10.5194/tc-11-2555-2017

Palm, S. P., Kayetha, V., & Yang, Y. (2018). Toward a Satellite-Derived Climatology of Blowing Snow Over Antarctica. *Journal of Geophysical Research: Atmospheres*, *123*(18), 10,301-10,313. https://doi.org/10.1029/2018JD028632

Pomeroy, J. W., & Male, D. H. (1988). OPTICAL PROPERTIES OF BLOWING SNOW. *Journal of Glaciology*, *116*, 3–10. https://doi.org/10.3189/S0022143000008996

Ritsche, M. T., & Prell, J. (2011). *ARM Surface Meteorology Systems Handbook* (No. DOE/SC-ARM/TR-086) (p. 19). Retrieved from https://www.arm.gov/publications/tech_reports/handbooks/met_handbook.pdf

Sassen, K. (1991). The Polarization Lidar Technique for Cloud Research: A Review and Current Assessment. *Bulletin of the American Meteorological Society*, *72*(12), 1848–4866. https://doi.org/10.1175/1520-0477(1991)072<1848:TPLTFC>2.0.CO;2

Scarchilli, C., Frezzotti, M., Grigioni, P., De Silvestri, L., Agnoletto, L., & Dolci, S. (2010). Extraordinary blowing snow transport events in East Antarctica. *Climate Dynamics*, *34*(7–8), 1195–1206. https://doi.org/10.1007/s00382-009-0601-0

Seefeldt, M. W., Tripoli, G. J., & Stearns, C. R. (2003). A High-Resolution Numerical Simulation of the Wind Flow in the Ross Island Region, Antarctica. *Monthly Weather Review*, *131*(2), 435–458. https://doi.org/10.1175/1520-0493(2003)131<0435:AHRNSO>2.0.CO;2

This article is protected by copyright. All rights reserved.

Accepted Article

Souverijns, N., Gossart, A., Lhermitte, S., Gorodetskaya, I. V., Kneifel, S., Maahn, M., et al. (2017). Estimating radar reflectivity - Snowfall rate relationships and their uncertainties over Antarctica by combining disdrometer and radar observations. *Atmospheric Research*, *196*, 211–223. https://doi.org/10.1016/j.atmosres.2017.06.001

Trouvilliez, A., Naaim-Bouvet, F., Genthon, C., Piard, L., Favier, V., Bellot, H., et al. (2014). A novel experimental study of aeolian snow transport in Adelie Land (Antarctica). *Cold Regions Science and Technology*, *108*, 125–138. https://doi.org/10.1016/j.coldregions.2014.09.005

Weber, N. J., Lazzara, M. A., Keller, L. M., & Cassano, J. J. (2016). The Extreme Wind Events in the Ross Island Region of Antarctica. *Weather and Forecasting*, *31*(3), 985–1000. https://doi.org/10.1175/WAF-D-15-0125.1

Yang, J., & Yau, M. K. (2011). A case study of blowing snow cooling effects on anticyclogenesis and cyclolysis. *Journal of Geophysical Research: Atmospheres*, *116*(D11). https://doi.org/10.1029/2010JD014624

This article is protected by copyright. All rights reserved.

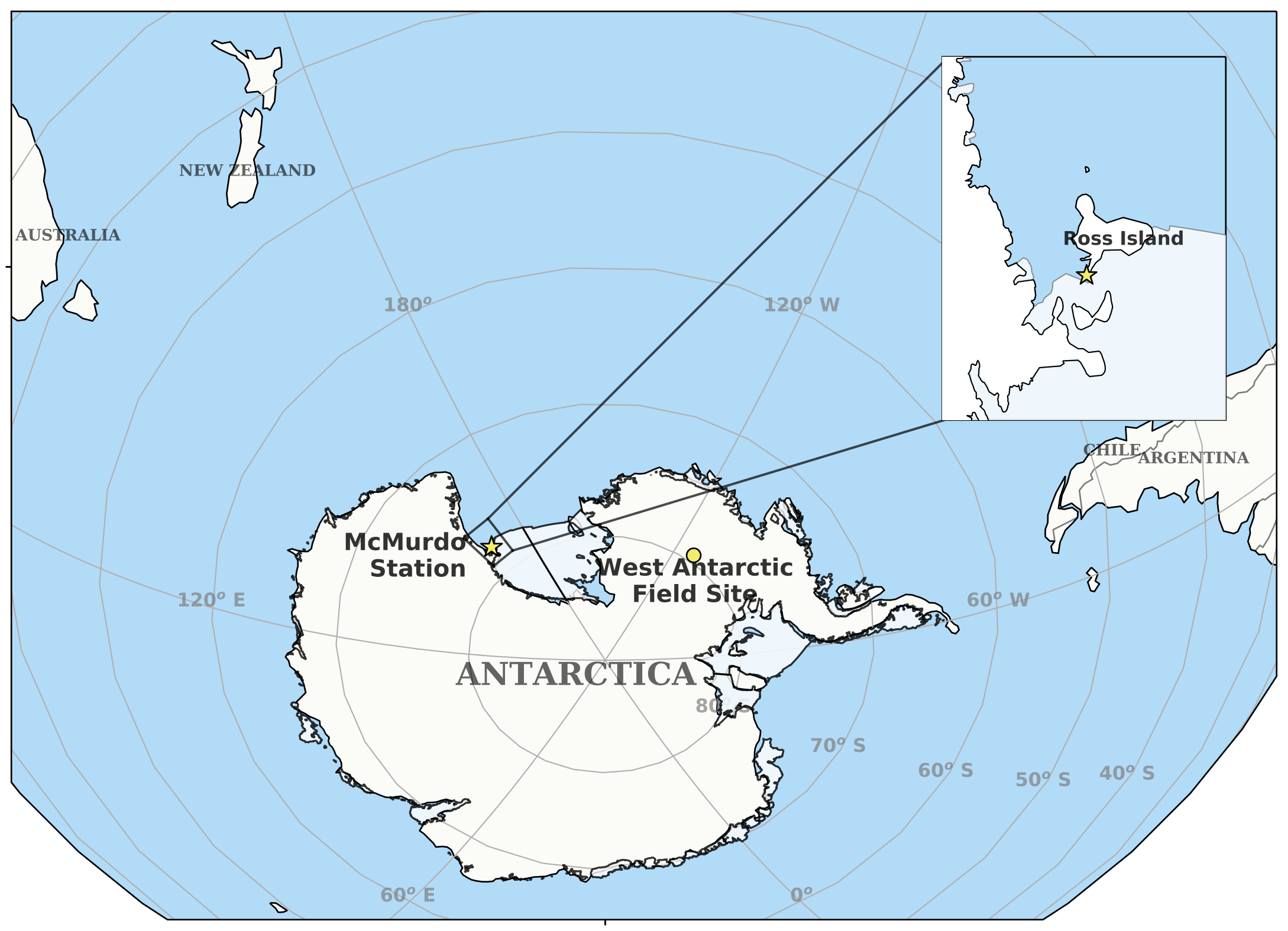
NEW ZEALAND
AUSTRALIA
180°
120° W
Ross Island
CHILE
ARGENTINA
McMurdo
Station
West Antarctic
Field Site
120° E
60° W
ANTARCTICA
80° S
70° S
60° S
50° S
40° S
60° E
0°

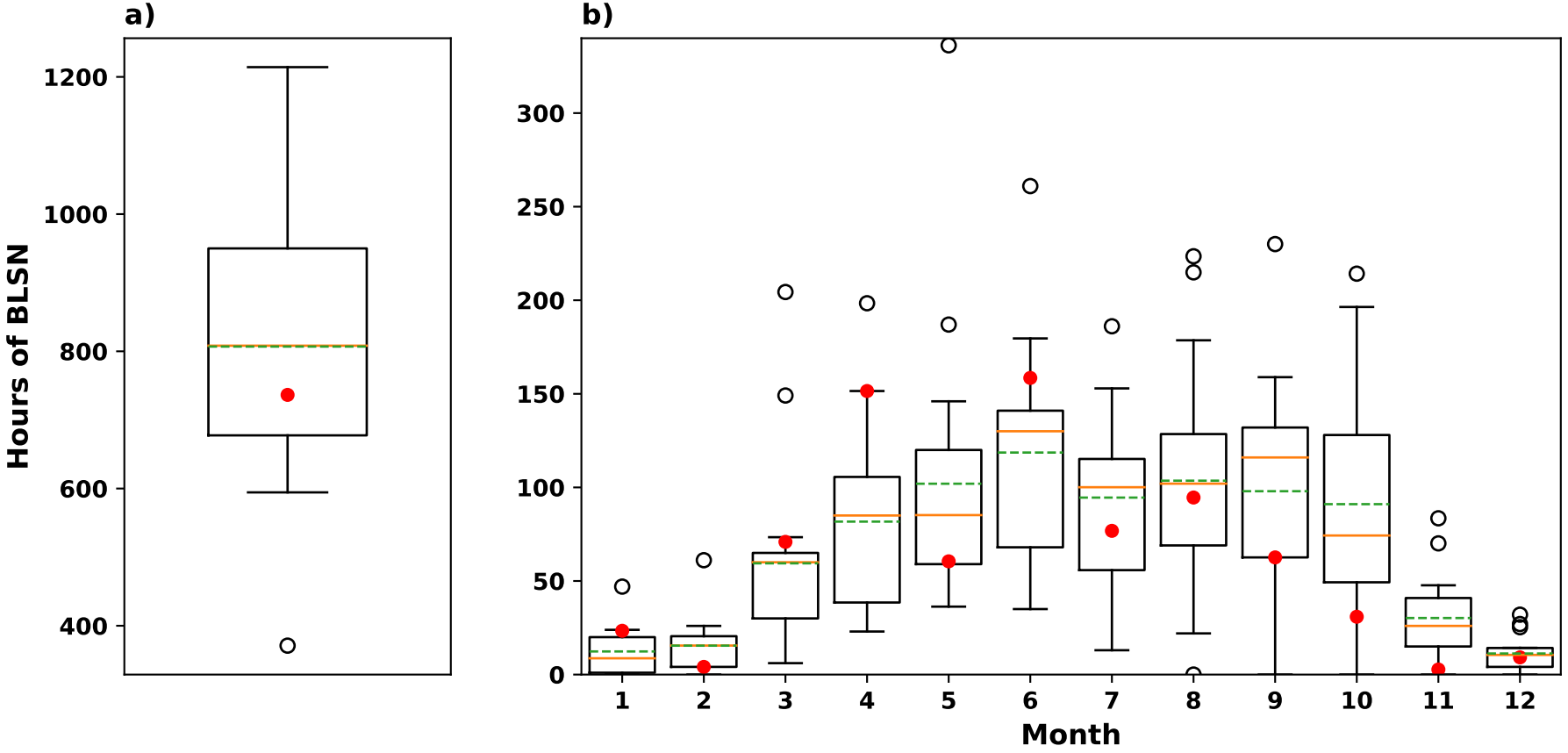
a)
b)
Hours of BLSN
1200
1000
800
600
400
300
250
200
150
100
50
0
1
2
3
4
5
6
7
8
9
10
11
12
Month

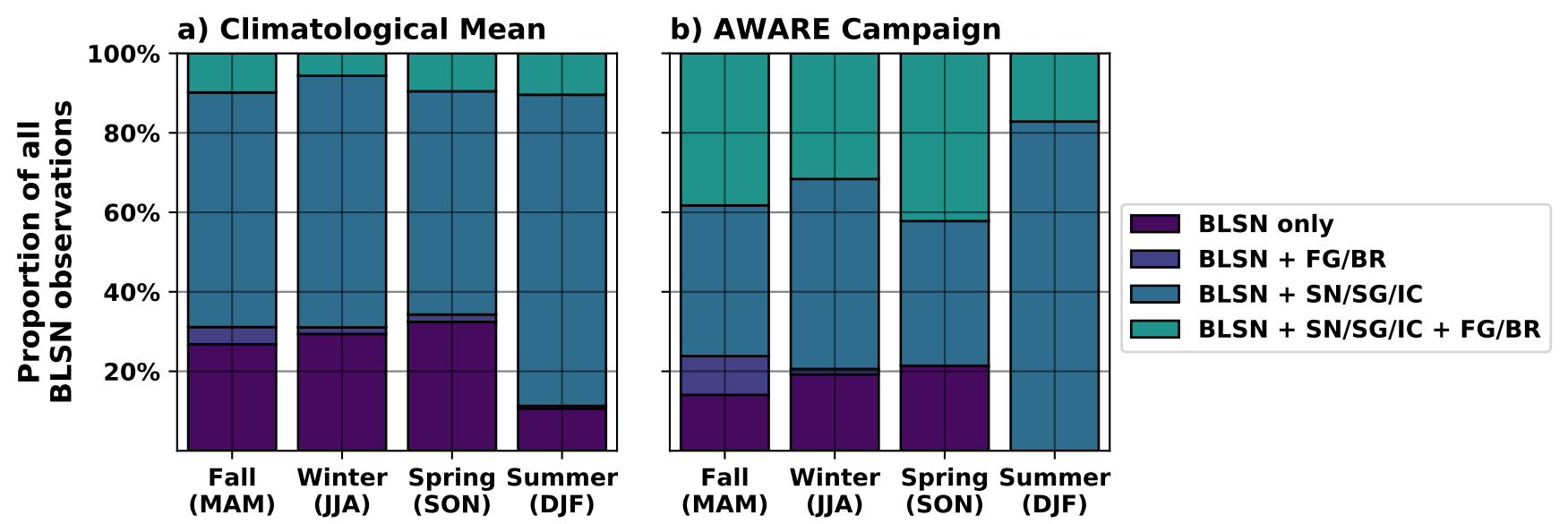
a) Climatological Mean
b) AWARE Campaign
Proportion of all BLSN observations
100%
80%
60%
40%
20%
Fall (MAM)
Winter (JJA)
Spring (SON)
Summer (DJF)
BLSN only
BLSN + FG/BR
BLSN + SN/SG/IC
BLSN + SN/SG/IC + FG/BR

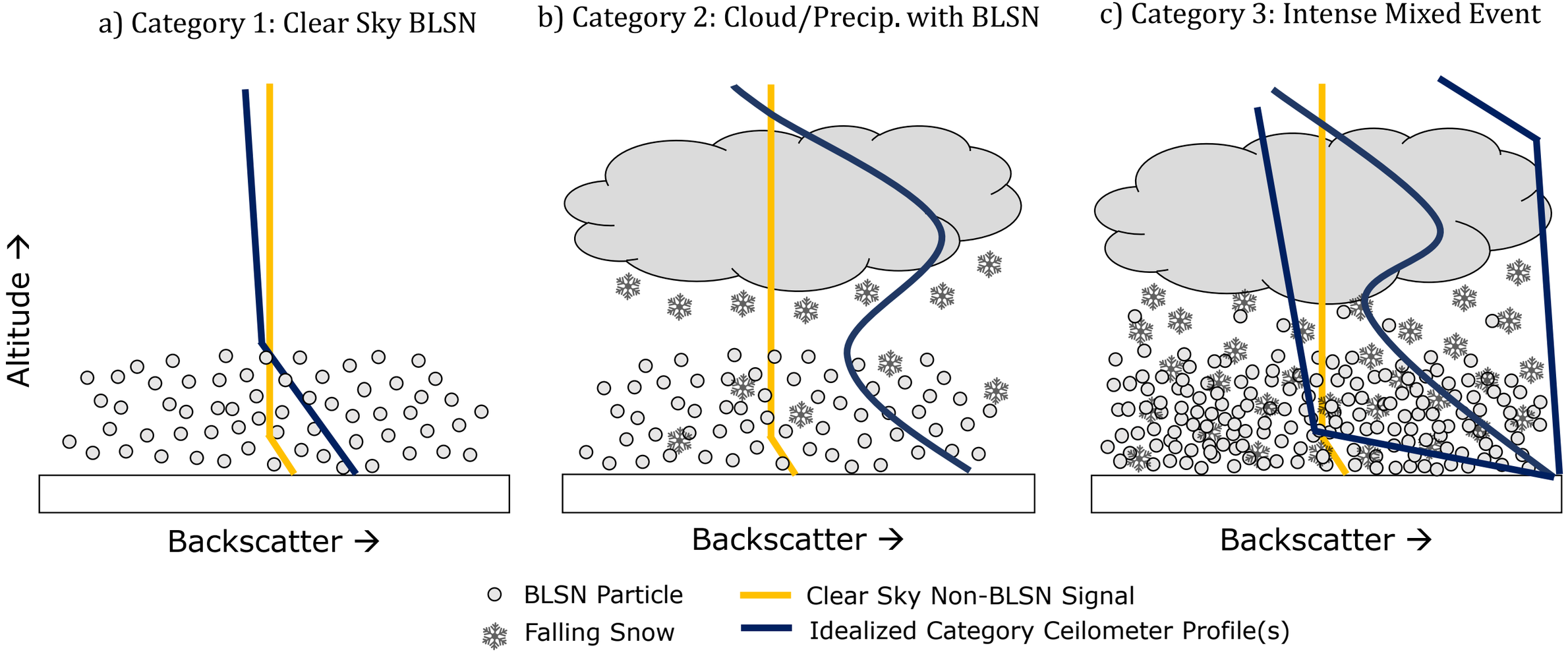
a) Category 1: Clear Sky BLSN
b) Category 2: Cloud/Precip. with BLSN
c) Category 3: Intense Mixed Event
Altitude →
Backscatter →
Backscatter →
Backscatter →
BLSN Particle
Falling Snow
Clear Sky Non-BLSN Signal
Idealized Category Ceilometer Profile(s)

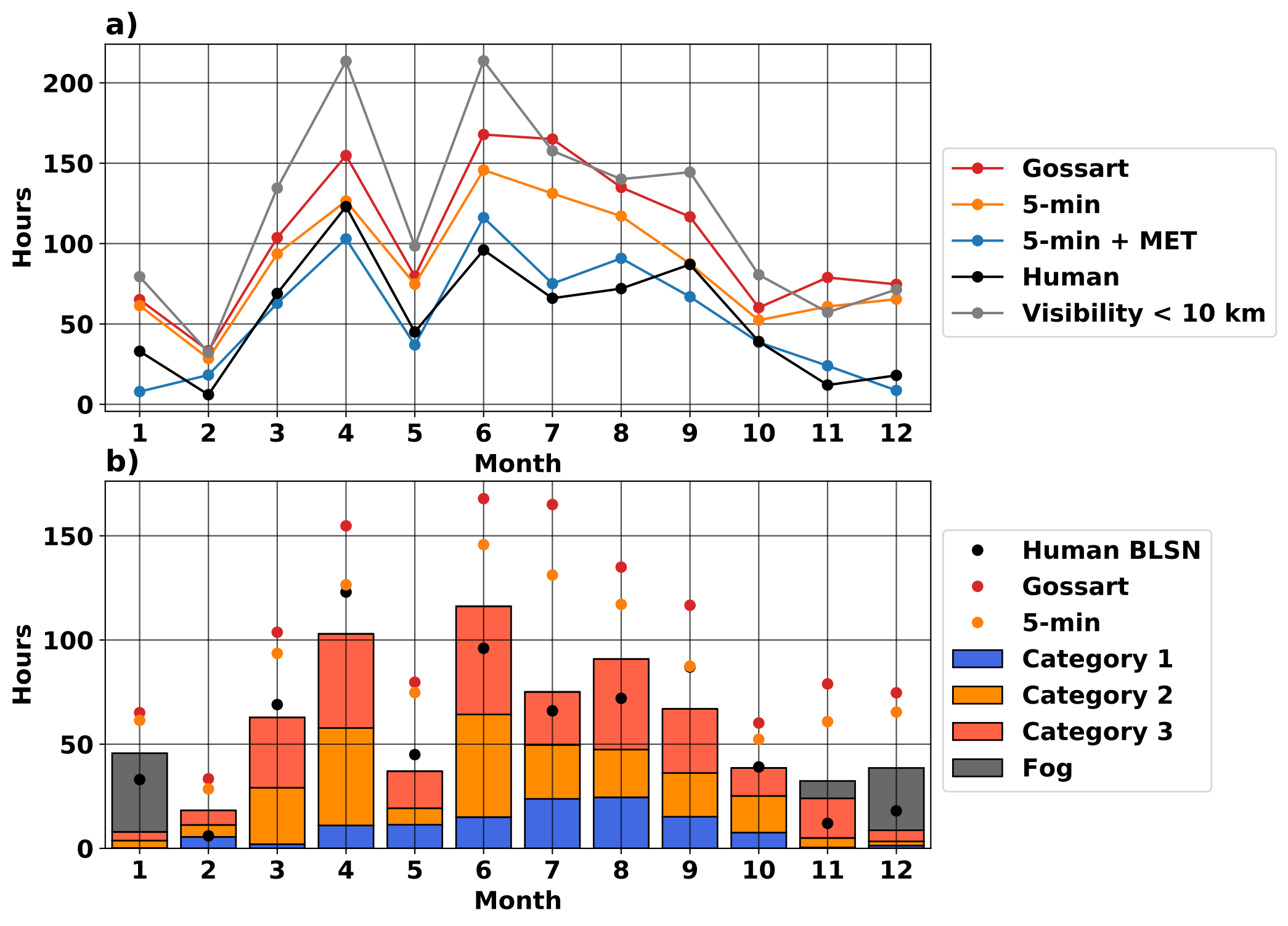
a)
Hours
Month
Gossart
5-min
5-min + MET
Human
Visibility < 10 km
b)
Hours
Month
Human BLSN
Gossart
5-min
Category 1
Category 2
Category 3
Fog

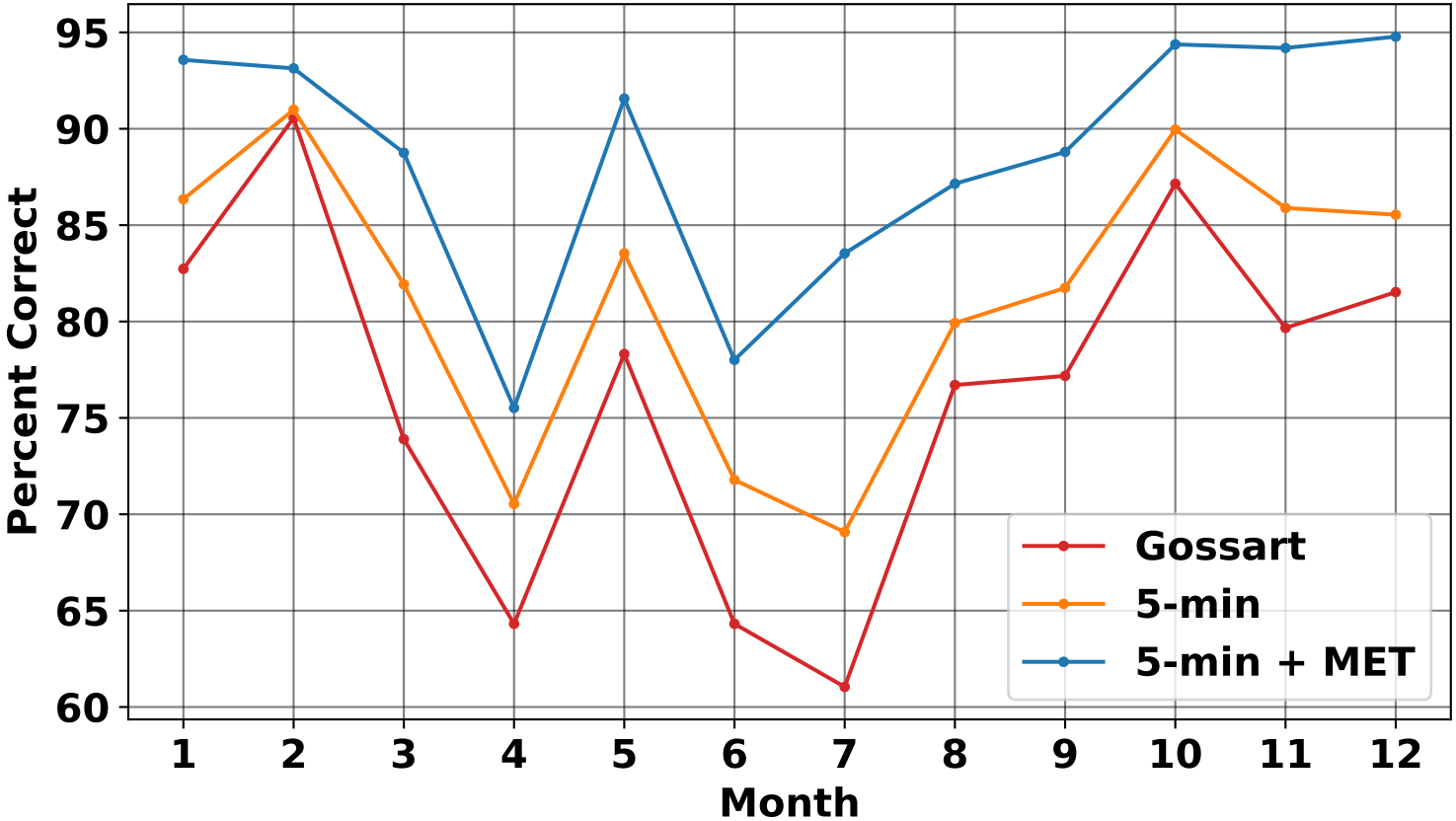
Percent Correct
95
90
85
80
75
70
65
60
1
2
3
4
5
6
7
8
9
10
11
12
Month
Gossart
5-min
5-min + MET

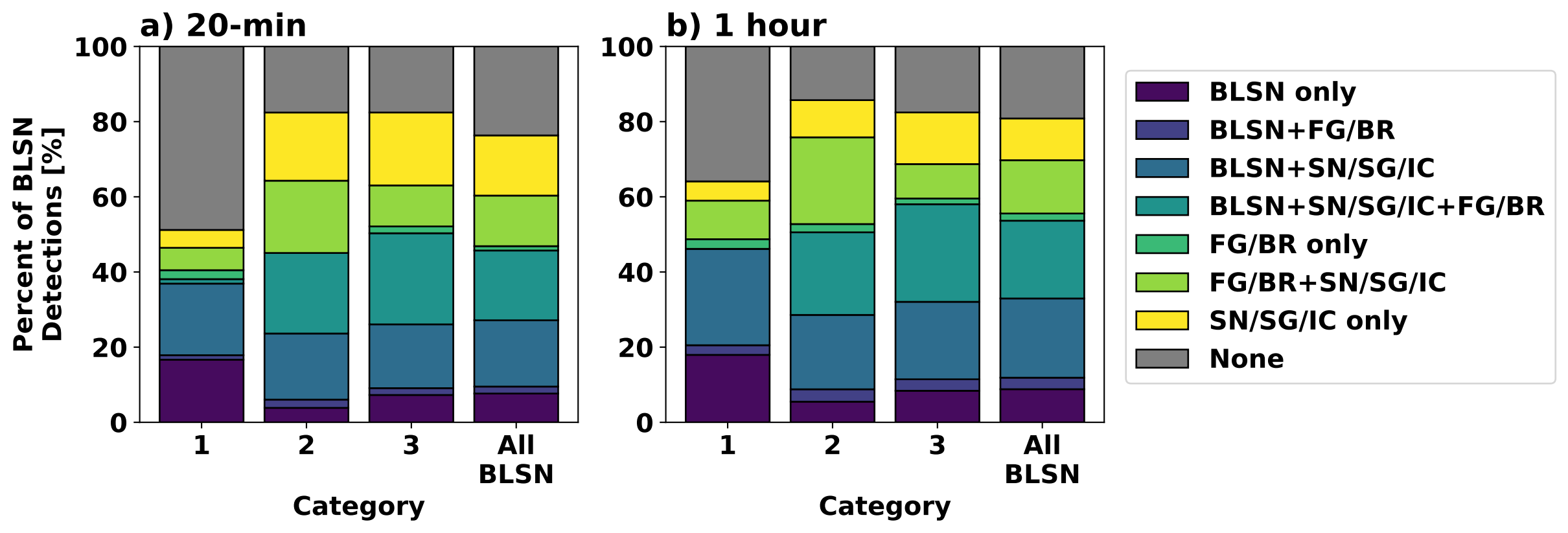
a) 20-min
b) 1 hour
Percent of BLSN Detections [%]
100
80
60
40
20
0
1
2
3
All BLSN
Category
BLSN only
BLSN+FG/BR
BLSN+SN/SG/IC
BLSN+SN/SG/IC+FG/BR
FG/BR only
FG/BR+SN/SG/IC
SN/SG/IC only
None

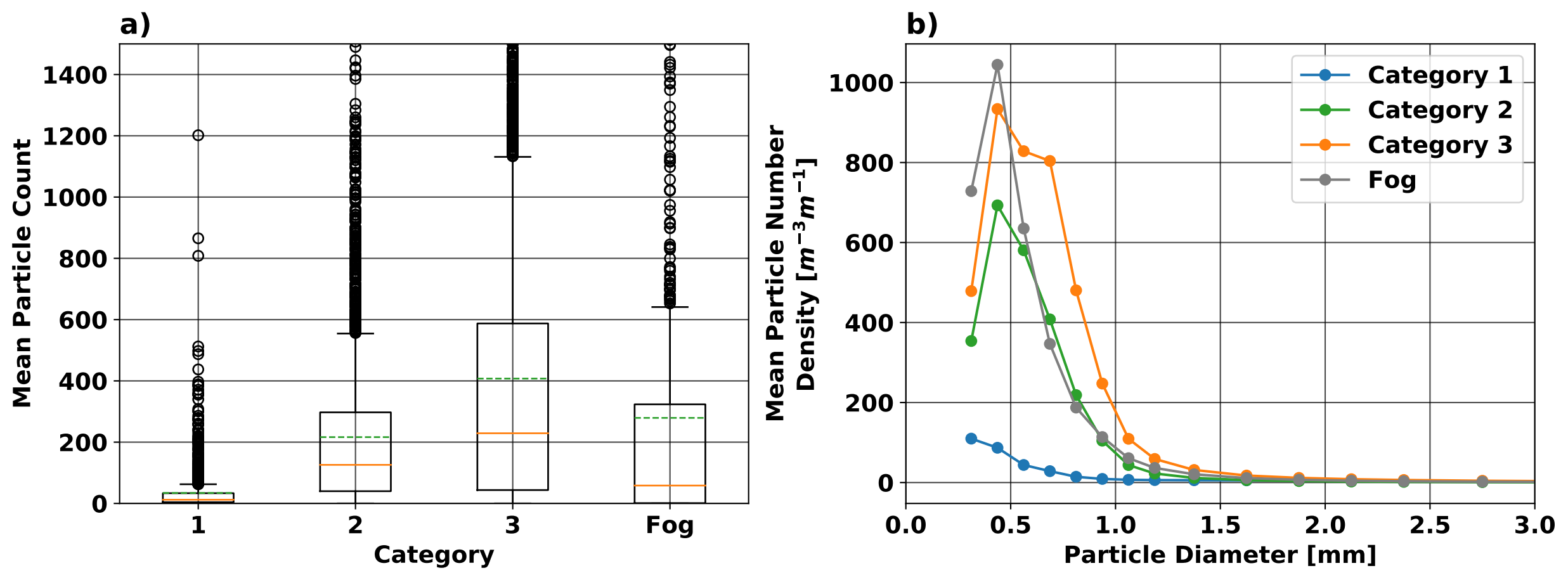
a)
Mean Particle Count
0
200
400
600
800
1000
1200
1400
1
2
3
Fog
Category
b)
Mean Particle Number Density [$m^{-3}m^{-1}$]
0
200
400
600
800
1000
0.0
0.5
1.0
1.5
2.0
2.5
3.0
Particle Diameter [mm]
Category 1
Category 2
Category 3
Fog

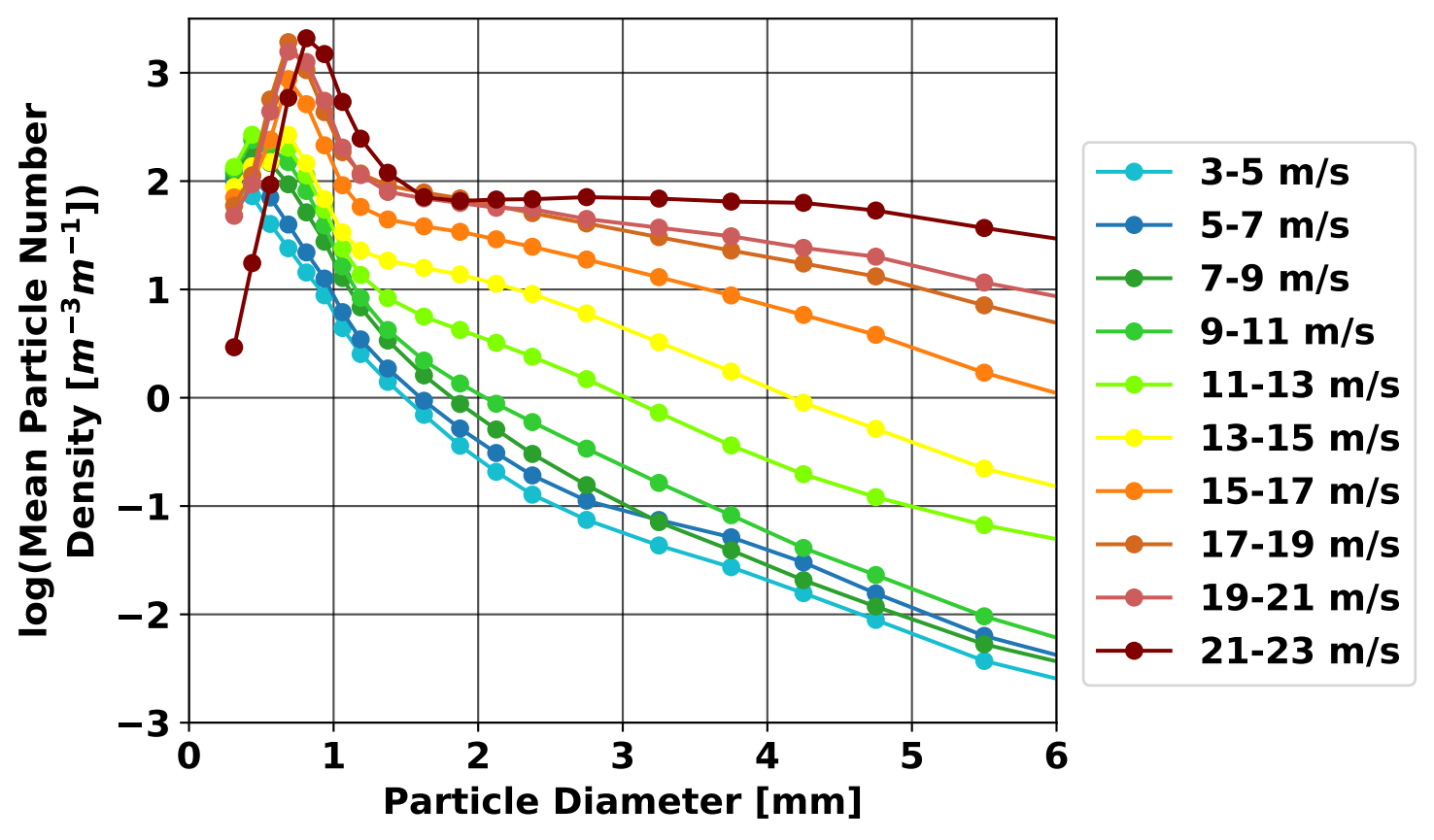
log(Mean Particle Number Density [$m^{-3}m^{-1}$])
3
2
1
0
−1
−2
−3
0
1
2
3
4
5
6
Particle Diameter [mm]
3-5 m/s
5-7 m/s
7-9 m/s
9-11 m/s
11-13 m/s
13-15 m/s
15-17 m/s
17-19 m/s
19-21 m/s
21-23 m/s

a) Visibility vs. Wind Speed

b) Visibility vs. Wind Speed

c) Wind Speed vs. Temperature

d) Wind Speed vs. Temperature

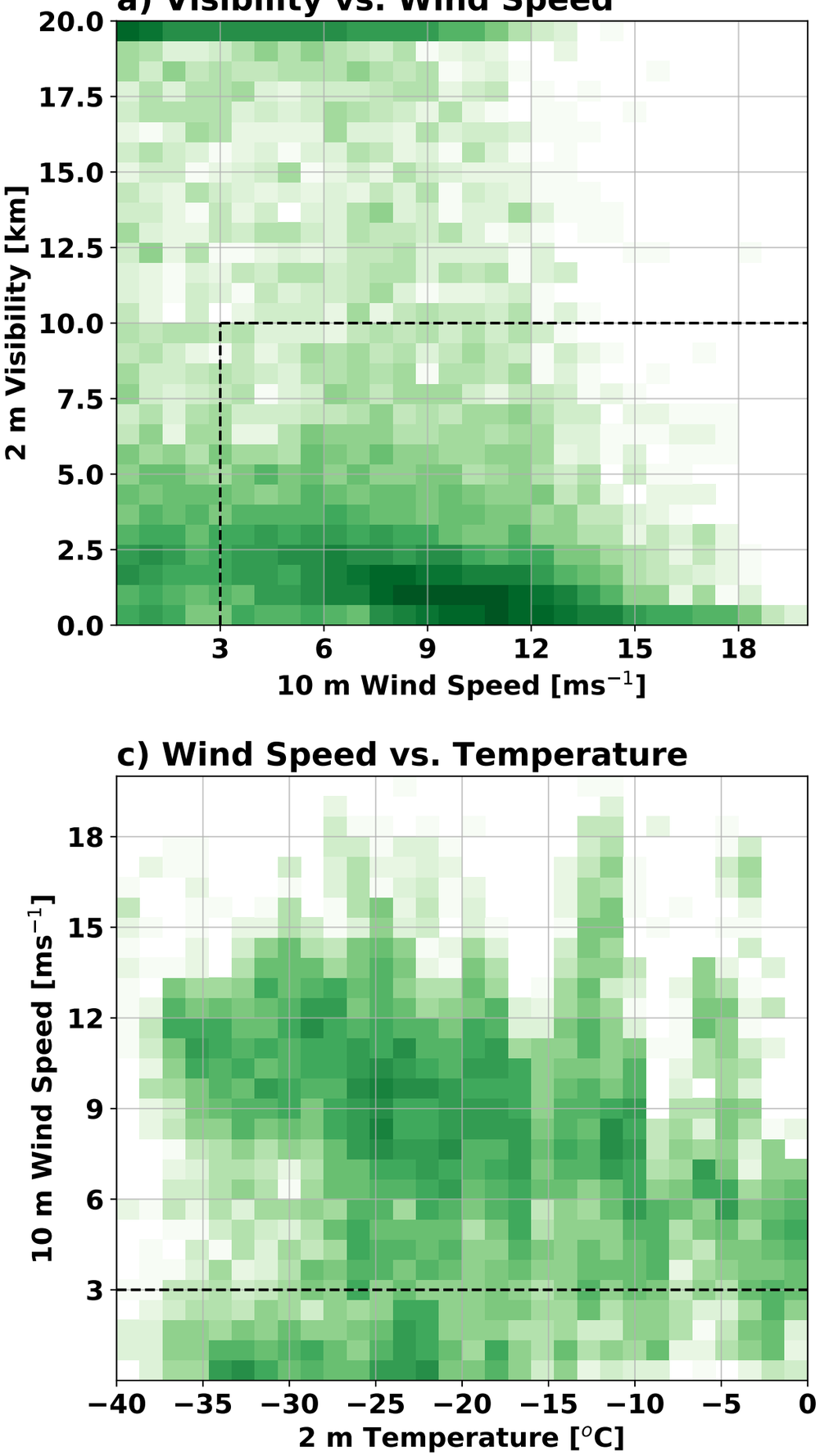

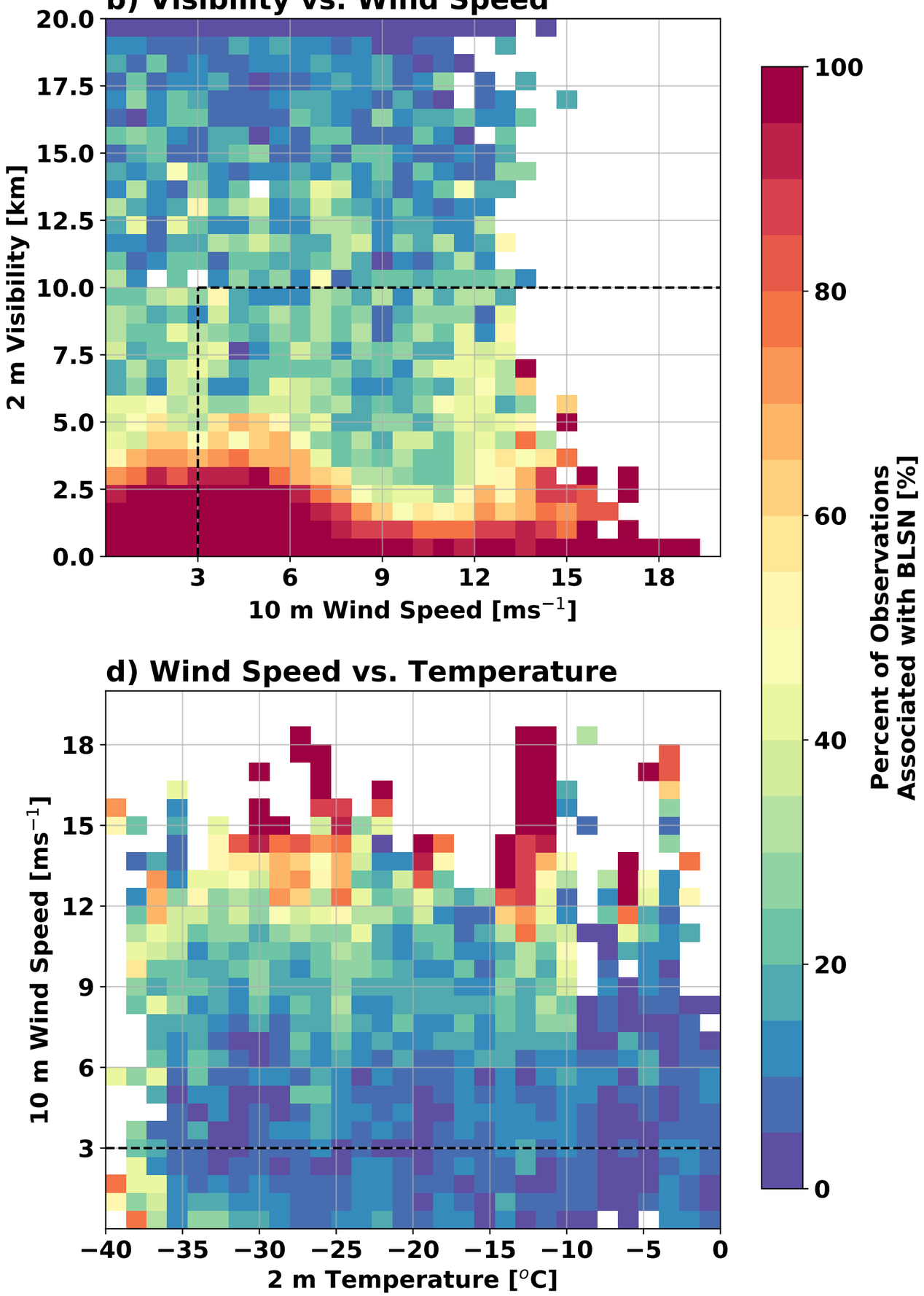

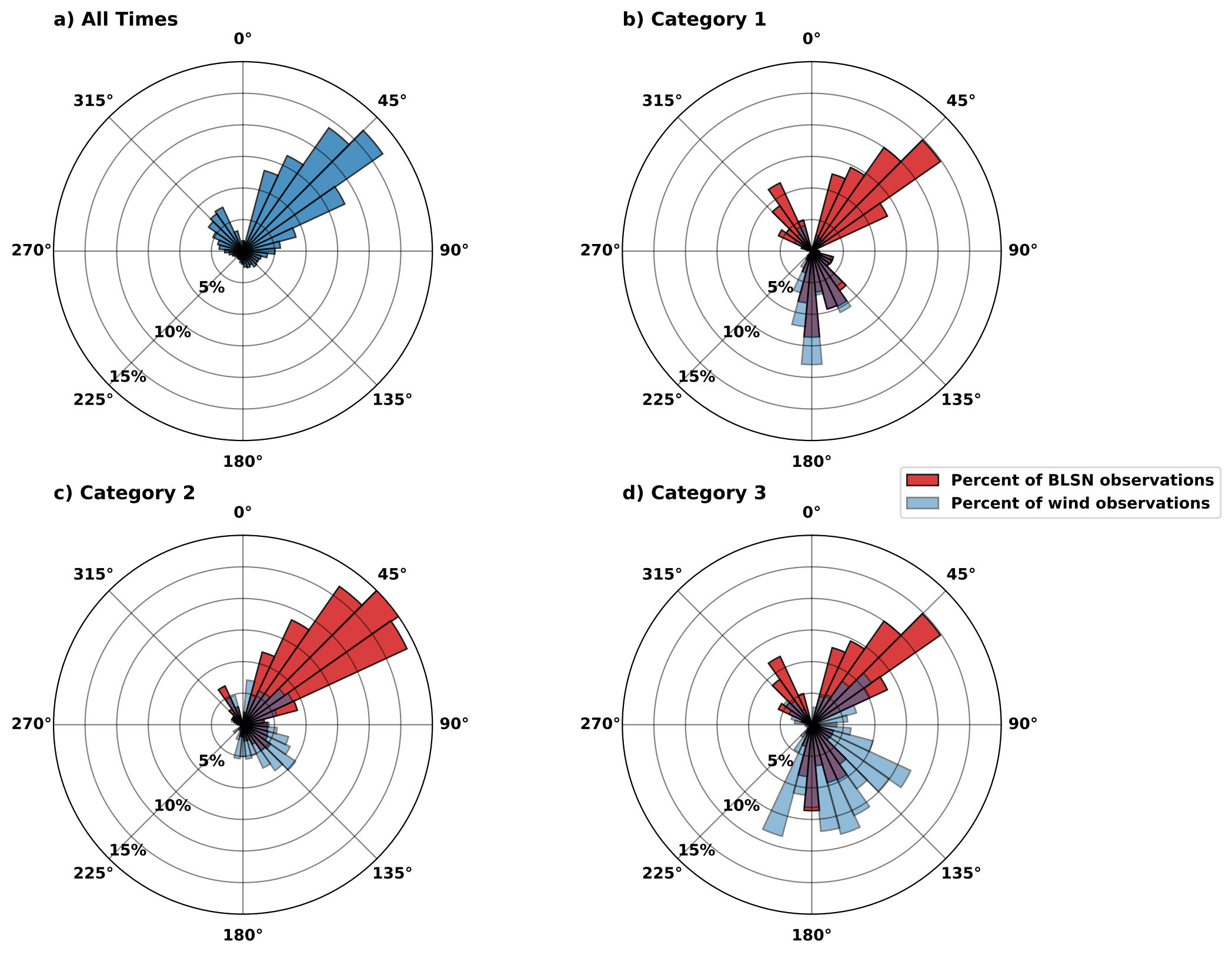
a) All Times
b) Category 1
c) Category 2
d) Category 3
0°
45°
90°
135°
180°
225°
270°
315°
5%
10%
15%
Percent of BLSN observations
Percent of wind observations

a) Human Observations

Human Observations

BLSN

FG/BR

SN/SG/IC

21:00 23:00 01:00 03:00 05:00 07:00 09:00

Hours observed (3 hr period)

0.0 0.5 1.0 1.5 2.0 2.5 3.0

b) Ceilometer Backscatter

Height AGL [m]

0 100 200 300 400 500

Category 1

Category 2

Category 3

log(Backscatter $[sr^{-1}km^{-1}10000^{-1}]$)

1.00 1.25 1.50 1.75 2.00 2.25 2.50 2.75 3.00

c) PARS Particle Number Density

Particle Size [mm]

0 1 2 3 4 5

log(Number Density $[m^{-3}mm^{-1}]$)

1.0 1.5 2.0 2.5 3.0 3.5

d) 10 m Wind, 2 m Visibility, 2 m Relative Humidity

Wind Speed $[ms^{-1}]$

0 5 10 15

Visibility $[km]$

0 5 10 15 20

Relative Humidity [%]

0 20 40 60 80 100

21:00 23:00 01:00 03:00 05:00 07:00 09:00

Time [UTC]

Human Observations

a) Human Observations

BLSN
FG/BR
SN/SG/IC

03:00 06:00 09:00 12:00 15:00 18:00 21:00 00:00

Hours observed (3 hr period)
3.0 2.5 2.0 1.5 1.0 0.5 0.0

b) Ceilometer Backscatter

Height AGL [m]
1500 1000 500 0

Category 1
Category 2
Category 3

log(Backscatter $[sr^{-1}km^{-1}10000^{-1}]$)
3.00 2.75 2.50 2.25 2.00 1.75 1.50 1.25 1.00

03:00 06:00 09:00 12:00 15:00 18:00 21:00 00:00

c) PARS Particle Number Density

Particle Size [mm]
5 4 3 2 1 0

log(Number Density $[m^{-3}mm^{-1}]$)
3.5 3.0 2.5 2.0 1.5 1.0

03:00 06:00 09:00 12:00 15:00 18:00 21:00 00:00

d) 10 m Wind, 2 m Visibility, 2 m Relative Humidity

Wind Speed $[ms^{-1}]$
15.0 12.5 10.0 7.5 5.0

Visibility $[km]$
20 15 10 5 0

Relative Humidity [%]
100 80 60 40 20 0

03:00 06:00 09:00 12:00 15:00 18:00 21:00 00:00

Time [UTC]

a) HSRL Backscatter

Height AGL [m]

1500
1000
500
0

03:00 06:00 09:00 12:00 15:00 18:00 21:00 00:00

log(Backscatter [$sr^{-1}km^{-1}10^{-4}$])

3.5 3.0 2.5 2.0 1.5 1.0

b) KAZR Reflectivity

Height AGL [m]

1500
1000
500
0

03:00 06:00 09:00 12:00 15:00 18:00 21:00 00:00

Reflectivity [dBZ]

0 −5 −10 −15 −20 −25 −30 −35 −40

c) HSRL Linear Depolarization Ratio

Height AGL [m]

1500
1000
500
0

03:00 06:00 09:00 12:00 15:00 18:00 21:00 00:00

Linear Depolarization Ratio

0.40 0.35 0.30 0.25 0.20 0.15 0.10 0.05 0.00

d) Color Ratio

Height AGL [m]

1500
1000
500
0

03:00 06:00 09:00 12:00 15:00 18:00 21:00 00:00

log(Color Ratio)

−4.50 −4.75 −5.00 −5.25 −5.50 −5.75 −6.00 −6.25 −6.50

a) Human Observations

Human Observations

BLSN

FG/BR

SN/SG/IC

05:00 06:00 07:00 08:00 09:00 10:00 11:00 12:00 13:00 14:00

Hours observed (3 hr period)

0.0 0.5 1.0 1.5 2.0 2.5 3.0

b) Gossart Algorithm, Ceilometer Backscatter

Height AGL [m]

0 100 200 300 400

Category 1

Category 2

Category 3

log(Backscatter $[sr^{-1}km^{-1}10000^{-1}]$)

1.00 1.25 1.50 1.75 2.00 2.25 2.50 2.75 3.00

05:00 06:00 07:00 08:00 09:00 10:00 11:00 12:00 13:00 14:00

c) 5-min Algorithm, Ceilometer Backscatter

Height AGL [m]

0 100 200 300 400

Category 1

Category 2

Category 3

log(Backscatter $[sr^{-1}km^{-1}10000^{-1}]$)

1.00 1.25 1.50 1.75 2.00 2.25 2.50 2.75 3.00

05:00 06:00 07:00 08:00 09:00 10:00 11:00 12:00 13:00 14:00

d) PARS Particle Number Density

Particle Size [mm]

0 1 2 3 4 5

log(Number Density $[m^{-3}mm^{-1}]$)

1.0 1.5 2.0 2.5 3.0 3.5

05:00 06:00 07:00 08:00 09:00 10:00 11:00 12:00 13:00 14:00

e) 10 m Wind, 2 m Visibility, 2 m Relative Humidity

Wind Speed $[ms^{-1}]$

0 5 10

Visibility $[km]$

0 5 10 15 20

Relative Humidity [%]

0 20 40 60 80 100

05:00 06:00 07:00 08:00 09:00 10:00 11:00 12:00 13:00 14:00

Time [UTC]

a) Human Observations

Human Observations

BLSN

FG/BR

SN/SG/IC

21:00 22:00 23:00 00:00 01:00 02:00 03:00 04:00

Hours observed (3 hr period)

0.0 0.5 1.0 1.5 2.0 2.5 3.0

b) Gossart Algorithm, Ceilometer Backscatter

Height AGL [m]

0 100 200 300 400

Category 1

Category 2

Category 3

log(Backscatter $[sr^{-1}km^{-1}10000^{-1}]$)

1.00 1.25 1.50 1.75 2.00 2.25 2.50 2.75 3.00

21:00 22:00 23:00 00:00 01:00 02:00 03:00 04:00

c) 5-min Algorithm, Ceilometer Backscatter

Height AGL [m]

0 100 200 300 400

Category 1

Category 2

Category 3

Fog

log(Backscatter $[sr^{-1}km^{-1}10000^{-1}]$)

1.00 1.25 1.50 1.75 2.00 2.25 2.50 2.75 3.00

21:00 22:00 23:00 00:00 01:00 02:00 03:00 04:00

d) PARS Particle Number Density

Particle Size [mm]

0 1 2 3 4 5

log(Number Density $[m^{-3}mm^{-1}]$)

1.0 1.5 2.0 2.5 3.0 3.5

21:00 22:00 23:00 00:00 01:00 02:00 03:00 04:00

e) 10 m Wind, 2 m Visibility, 2 m Relative Humidity

Wind Speed $[ms^{-1}]$

0 5 10 15

Visibility $[km]$

0 5 10 15 20

Relative Humidity [%]

0 20 40 60 80 100

21:00 22:00 23:00 00:00 01:00 02:00 03:00 04:00

Time [UTC]

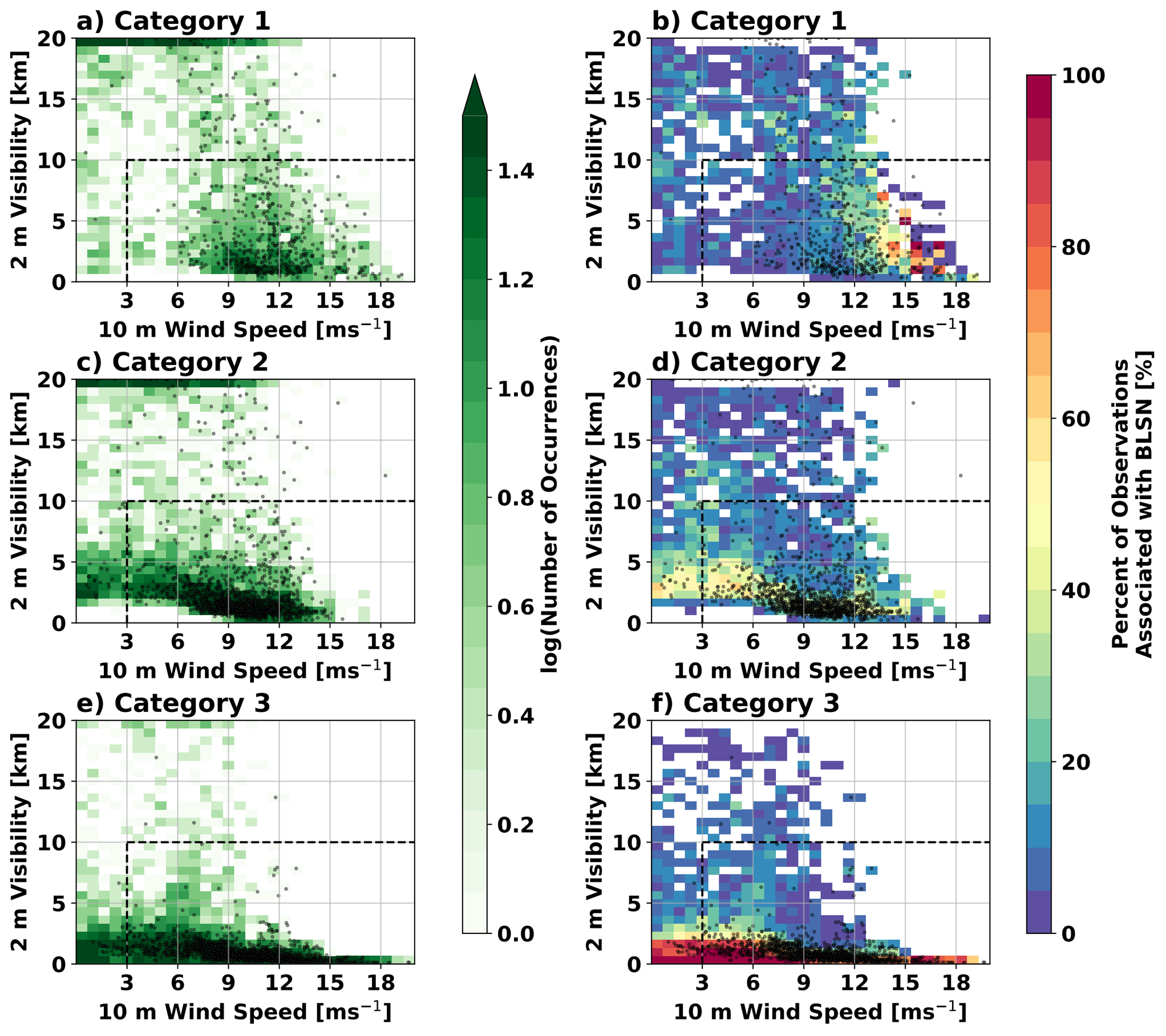
a) Category 1
b) Category 1
c) Category 2
d) Category 2
e) Category 3
f) Category 3
2 m Visibility [km]
10 m Wind Speed [ms^{-1}]
log(Number of Occurrences)
Percent of Observations Associated with BLSN [%]

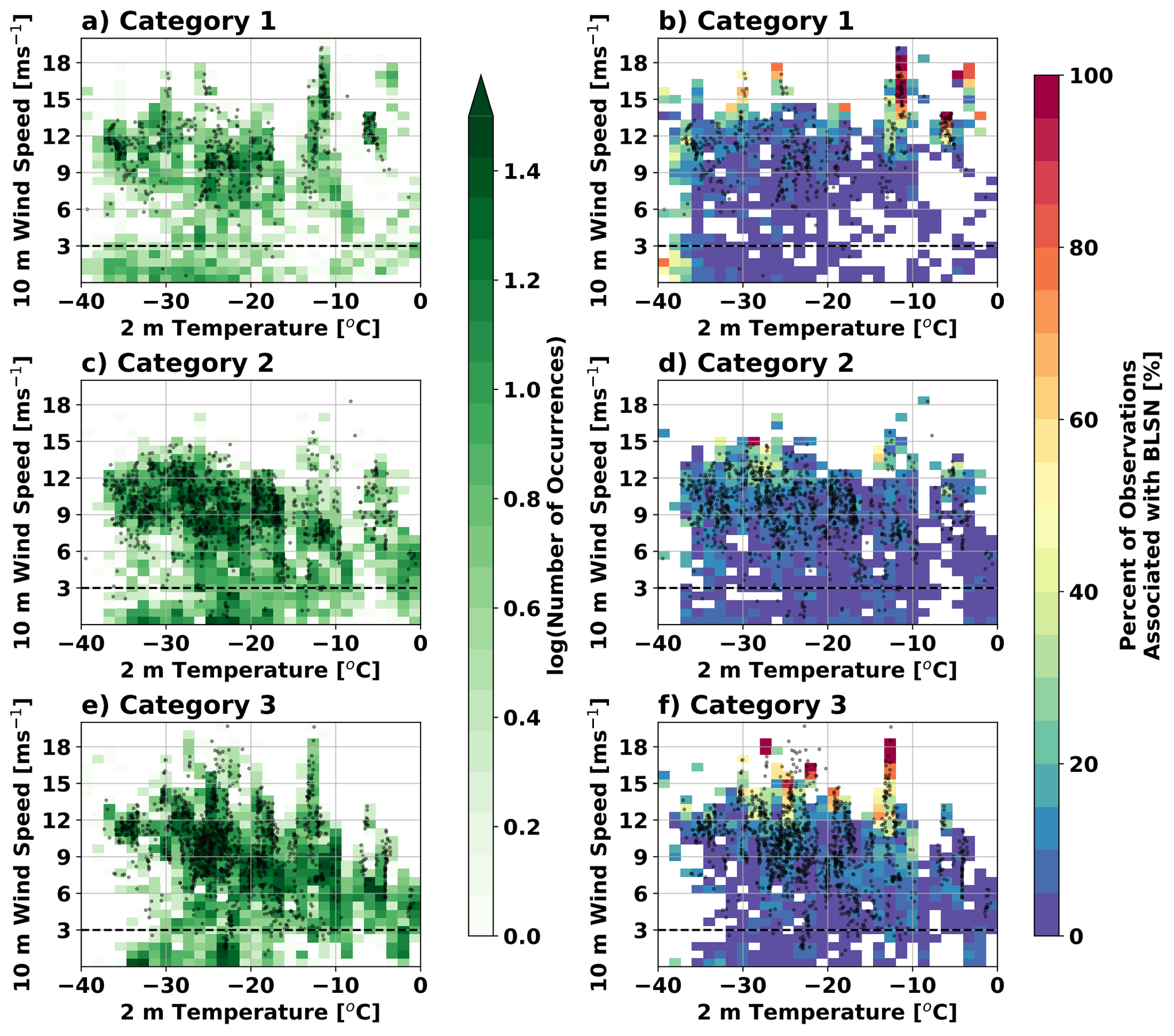
a) Category 1
b) Category 1
c) Category 2
d) Category 2
e) Category 3
f) Category 3
10 m Wind Speed [ms^{-1}]
2 m Temperature [^{o}C]
log(Number of Occurrences)
Percent of Observations Associated with BLSN [%]